Supplementary Information (SI) for Journal of Materials Chemistry A.

Achieving high current density, high areal capacity, and high DOD AZIBs by screening amino acids

Jianghui Cao [a, e], Zhen Yuan [a], Chengjie Li [b,*], Fang Zhao [a], Qidong Zhao [a], Liguo Gao [a], Tingli Ma [d], Xuefeng Ren [a,*], Xifei Li [c, *] and Anmin Liu [a,*]

[a] School of Chemical Engineering, Ocean and Life Sciences; Leicester International Institute, Dalian University of Technology, Panjin 124221, China.

E-mail: liuanmin@dlut.edu.cn; renxuefeng@dlut.edu.cn

[b] Shandong Engineering Research Center of Green and High-value Marine Fine Chemical, Weifang University of Science and Technology, Weifang 262700, China.

E-mail: cjli@wfust.edu.cn

[c] Key Materials & Components of Electrical Vehicles for Overseas Expertise Introduction Center for Discipline Innovation, Institute of Advanced Electrochemical Energy & School of Materials Science and Engineering, Xi'an University of Technology, Xi'an, Shaanxi 710048, PR China

E-mail: xfli@xaut.edu.cn

[d] Department of Materials Science and Engineering, China Jiliang University, Hangzhou, 310018, China.

[e] Department of Chemistry, National University of Singapore, Singapore, 117546, Singapore.

Chemical and Materials

Reagent names	Purity	Manufacture
N-methyl pyrrolidone (NMP)	analytical purity	Shanghai Aladdin Biochemical Technology Co., Ltd.
Potassium permanganate	99%	Shanghai Aladdin Biochemical Technology Co., Ltd.
Manganese sulphate monohydrate	99%	Shanghai Aladdin Biochemical Technology Co., Ltd.
Zinc sulfate heptahydrate	99%	Shanghai Aladdin Biochemical Technology Co., Ltd.
L-histidine	99%	Shanghai Aladdin Biochemical Technology Co., Ltd.
L-arginine	99%	Shanghai Aladdin Biochemical Technology Co., Ltd.
L-glutamic acid	99%	Shanghai Aladdin Biochemical Technology Co., Ltd.
L-serine	99%	Shanghai Aladdin Biochemical Technology Co. Ltd.
Zinc metal foil	99.99%	Guangdong Canrd New Energy Technology Co., Ltd.
Copper metal foil	99.99%	Guangdong Canrd New Energy Technology Co., Ltd.
battery case	Battery level	Guangdong Canrd New Energy Technology Co., Ltd.
graphitized carbon black	99%	Shanghai Aladdin Biochemical Technology Co., Ltd.
PVDF	99%	Shanghai Aladdin Biochemical Technology Co., Ltd.

Physical Characterisation Methods

X-ray diffraction (XRD-7000S, Shimadzu, Japan) can be used to characterize the crystalline structure of solid materials. The peaks of the diffraction spectra can be compared with JCPDS cards to obtain the structural composition of the corresponding materials. In this thesis, the spectra were obtained by scanning with an XRD diffractometer at a speed of 5° min^{-1} and an angular range of 5°−80° to study the zinc cathode, the by-products on the surface of the zinc cathode, and the cathode materials. Scanning Electron Microscopy (SEM) (Nova NanoSEM450, FEI company) is a characterization method used to observe the surface morphology of objects. In this thesis, the surface morphology of the zinc anode before and after cycling and the surface morphology of the cathode material are mainly characterized to obtain SEM images and atomic force microscopy (AFM) (Dimension ICON, Bruker) images at various scales. Fourier Transform infrared spectroscopy (FT-IR) can be used to characterize the molecular functional groups of substances (114899, Perkin Elmer Instruments). Prior to testing, the dispensing testing solution is then scanned and analyzed in a specific wavelength range. X-ray Photoelectron Spectroscopy (XPS) (ESCALAB™ 250Xi, ThermoFisher) can be used to study the elemental composition and content, chemical state, molecular structure, and chemical bonding of various compounds in the test samples. In this paper, XPS is mainly used to test the composition of Zn flakes after cycling. Raman spectroscopy (inVia, Renishaw) was used to investigate the surface of zinc foils after cycled in different electrolyte systems.

Electrochemical Performance Test

Cyclic Voltammetry

Cyclic voltammetry (CV) is a method to characterize the electrode materials and observe the redox reactions of the active materials and electrodes, and the CV curve reflects the kinetics of the electrode electrochemical reaction process. The kinetics of the reaction can be used to judge the reversibility of the electrode electrochemical reaction. In this paper, cyclic voltammetry was used to characterize the Zn negative electrode and positive electrode respectively, and the cyclic voltammetry scanning was carried out on the Zn//Zn, Zn//Cu cell using an electrochemical workstation (CHI630E, Shanghai Chenhua Instruments Co., Ltd) in order to study the nucleation behavior of the Zn negative electrode and the reversibility of electrochemical reactions. We also tested the performance of Zn//MnO_2. In addition, cyclic voltammetry scans were performed over the voltage range of the cell when the zinc was paired with the positive electrode as the negative electrode to study the reaction process of the zinc ion batteries.

Chronoamperometry

Chronoamperometry (CA), is a transient test method that discusses the relationship between current and time. The ionic diffusion behavior at the electrode surface can be investigated by initial voltage polarization. The time-current curve of a Zn//Zn cell was tested using a step voltage of −20 mV for a duration of 300 s.

Linear Sweep Voltammetry

Linear sweep voltammetry (LSV) is a common electrochemical test method to record the relationship between current and electrode potential. In this paper, LSV was used to test the extent of hydrogen precipitation reaction on the surface of the zinc negative electrode, and we tested in the Zn//SS system.

Galvanostatic Charge/Discharge Electrochemical Test

The galvanostatic charge/discharge (GCD) electrochemical test (CT2001A, Wuhan LAND Electronic Co., Ltd) is an electrochemical method to investigate the cycling stability of zinc anode, the nucleation behavior of zinc, and the electrochemical performance of zinc ion batteries. In this paper, Zn//Zn symmetric and Zn//Cu batteries were subjected to constant-current charge/discharge tests to investigate the cycling stability of the Zn negative electrode and the nucleation behavior of Zn. In addition, constant current charge/discharge tests were performed over the operating voltage range to investigate the electrochemical properties of the Zn-ion batteries. The constant current charge/discharge tests were performed at 25°C for all cells.

Electrochemical Impedance Spectroscopy

Electrochemical Impedance Spectroscopy (EIS) is a method of obtaining impedance spectra by measuring the voltage (current) changes in a sinusoidal trend of the current (voltage). The EIS reflects the correlation between the current and potential of the electrode. The EIS of the electrode is an important means of studying the ion transport mechanism at the electrode/electrolyte interface by fitting the obtained data to obtain the charge diffusion impedance and charge transport impedance. In this paper, the EIS tests were performed on a force-feeding electrochemical workstation at a frequency of 10^{-2}–10^5 Hz and an amplitude of 5 mV, where R_s is the ohmic impedance of the cell and R_{ct} represents the interfacial charge transport impedance in the equivalent circuit diagram.

Tafel Curve

The Tafel curve test is also a steady-state polarisation test method to discuss the relationship between current and voltage. The Tafel curves of the zinc negative electrode under different electrolyte systems were measured using a three-electrode system consisting of a zinc sheet as the study electrode, a platinum sheet as the counter electrode, and Ag/AgCl as the reference. The voltage range was −1.4 V~−0.6 V, and the scanning rate was 1.0 mV s^{-1}.

Preparation of the Electrolytes

The 1M $ZnSO_4$ (ZSO) electrolyte was formulated by dissolving 2.875 g of ZSO into 10 mL of pure water (Hangzhou Wahaha Group Co., Ltd), which was regarded as the baseline electrolyte. The ZSO electrolyte with different amino acids was prepared, 0.1M for arginine (Arg) and 0.02M for histidine (His).

Preparation of MnO_2

In a typical synthesis of MnO_2, 0.507 g $MnSO_4 \cdot H_2O$ was dissolved into deionized water (90 mL). 2 mL of 0.5 M sulfuric acid solution and 20 mL 0.1 M $KMnO_4$ solution were slowly added into the above solution and thoroughly stirred for 30 min. The solution was then transferred to a vacuum oven and heated at 120 °C for 12 h. After cooling down to room temperature, the obtained material was washed six times with deionized water and alcohol and dried using a freeze drier. The MnO_2 cathode was prepared as follows. MnO_2, SP, and PVDF were mixed in a weight ratio of 7:2:1, followed by adding NMP to get a uniform slurry. The slurry was cast on a stainless-steel foil cloth through an automatic coating machine and dried at 80 °C overnight.

Computational Details

Molecular Dynamic Simulation

The molecular simulation aims to build a solvation model of 1M and 5M ZSO, containing additive molecules. The additive's concentration varies from 0.1M, 0.15M to 0.2M. After that, the solvation structure can be divided from the solution model. The density of the solution model is set to be 1.2 g/cm^3. When the concentration of ZSO is 1M, and the additive is 0.2M, the solution consists of 50 Zn^{2+}, 50 SO_4^{2-}, 2778 H_2O, and additives. The same for other concentration models.

For each simulation, energy minimization was first employed to relax the simulation box. Then, a microcanonical (NVE) ensemble with a 1.0 fs time step and a total simulation time of 100 ps is employed to optimize the simulation box. The temperature of the systems is set to 298K. Next, an isenthalpy and isobaric (NPH) ensemble is introduced, with a 1.0 fs time step and a total simulation time of 100 ps, under the conditions of 0.1 GPa and 298 K. Following the NPH simulation, a canonical (NVT) ensemble with 100ps was operated to further optimize the simulation box, the time step is set to 1.0 fs. In all the MD simulations, the motion of atoms was described by classical Newton's equation. In the EDL model, there are 800 zinc atoms to simulate the zinc anode, and the total simulated time is 900ps.

Density Functional Theory Calculation

Utilizing the DMol3 module in the Materials Studio (MS) program, energy calculations and optimization of molecule structures using the DFT method were carried out. The generalized gradient approximations (GGA) of the Becke–Lee–Yang–Parr gradient correction (BLYP) approach with the core treatment of DFT Semi-core Pseudopots were carried out to visualize the frontier molecular orbitals and molecular electrostatic potential (MEP). Moreover, a series of methods can be applied to compute the solvation energy and binding energy. The solvation energies were produced based on the solvation structure separated from the liquid model of MD simulation, the calculation formula is (1). The binding energies (E_b) were counted on account of the bond of zinc-amino acids and zinc-H_2O, which are the composition of solvation structures. The computing equation is (2).

$Solvation\ energy$:

$$E_{solvation\ energy} = E_{solvation\ structure} - E_{Zn^{2+}} - nE_{amino\ acid} - mE_{H_2O} \qquad (1)$$

$Binding\ energy$:

$$E_{b(Zn^{2+}-H_2O)} = E_{Zn^{2+}-H_2O} - E_{Zn^{2+}} - E_{H_2O}$$

$$E_{b(Zn^{2+}-amino\ acid)} = E_{Zn^{2+}-amino\ acid} - E_{Zn^{2+}} - E_{amino\ acid} \qquad (2)$$

The adsorption model has been geometry pre-optimized by the Forcite program, and DMol3 optimization was called in the second step. The absorption energies and electron transfer numbers between additives and zinc anode surface were calculated using GGA with BLYP, together with the core treatment of all electrons. For electronic self-consistent and forces on atoms, cutoff quality was chosen at a high level, and the convergence accuracy is 1.0e^{-5} Ha and 0.002 Ha/Å, respectively. The fine quality of Brillouin zones was used to create a k-point mesh. A vacuum layer with a thickness of 20 Å was added to the supercell, which was constructed using the Zn (002) surface to generate a 4*4 supercell with four atom layers. To maintain the bulk property during relaxation, at least the lowest two layers of atoms were fixed. Calculations of the adsorption behavior of different amino acids on zinc slab have emerged. The variation in charge density was also visualized. The following equation (3) was used to compute the absorption energy (E_{abs}):

$$E_{abs} = E_{amino\ acid + Zn(002)} - E_{amino\ acid} - E_{Zn(002)} \qquad (3)$$

The Principle of Hydrogen Evolution Reaction

In the general Hydrogen Evolution Reaction (HER), the initial step involves the Volmer reaction (equations 1 and 2), wherein a proton combines with an electron to form an adsorbed hydrogen atom (H*) on the surface of the electrode material (M). Protons are typically sourced from the hydronium cation (H_3O^+) in acidic electrolytes or from water molecules in alkaline electrolytes. Subsequently, the formation of H_2 may proceed via the Heyrovsky reaction (equations 3 and 4) or the Tafel reaction (equation 5), or a combination of both. In the Heyrovsky step, an additional proton diffuses to the H* species, followed by its reaction with a second electron to generate H_2. On the other hand, the Tafel step involves the combination of two H* species on the electrode surface to produce H_2. [1–7]

(1) electrochemical hydrogen adsorption (Volmer reaction) (eqs 1 and 2)

$$H_3O^+ + M + e^- \rightleftharpoons M - H^* + H_2O\ (acidic\ medium)$$

(2) electrochemical desorption (Heyrovsky reaction) (eqs 3 and 4)

$H^+ + e^- + M - H^* \rightleftharpoons H_2 + M$ (acidic medium)

(3) chemical desorption (Tafel reaction) (eqs 5 and 6)

$2M - H^* \rightleftharpoons H_2 + 2M$ (both acidic and alkaline medium)

According to Sabatier's principle, catalysts exhibiting good HER activity should bond with the hydrogen atom neither too strongly nor too weakly. When the hydrogen atom bonds too weakly to the surface, the H adsorption step (Volmer) becomes difficult to occur. Conversely, if the hydrogen bonds too strongly to the surface, the desorption step (Heyrovsky/Tafel) becomes challenging. An optimal value for ΔG_{H*}~0 is considered ideal for achieving good HER activity from a thermodynamic perspective.

The hydrogen adsorption energies (ΔE_{H*}) are defined as formula (4)[8–12]:

$$\Delta E_{H^*} = \frac{E_{nH^*} - E_{Zn} - \frac{n}{2}E_{H_2}}{n} \qquad (4)$$

where E_{nH^*} is the total energy of the slab with nH atoms adsorbed, E_{Zn} is the energy of the Zn slab model, and E_{H_2} is the energy of the H_2 molecule in the gas phase state.

The hydrogen adsorption free energies (ΔG_{H^*}) were calculated based on formula (5):

$$\Delta G_{H^*} = \Delta E_{H^*} + \Delta ZPE - T\Delta S = \Delta E_{H^*} + ZPE_{H^*} - \frac{1}{2}ZPE_{H_2} - TS_{H^*} + \frac{1}{2}TS_{H_2} \quad (5)$$

where the ΔE_{H*} is defined in formula (4). The temperature is set to 300 K. The ZPE_{H*}, S_{H*}, ZPE_{H2}, and S_{H2} are the zero-point vibration energy and entropy of H that adsorbed on Zn surface and gas phase H_2 under standard atmospheric pressure, respectively.

The Depth of Discharge (DOD) Calculation

$$DOD = \frac{3.6XM}{\rho N_A nel} \times 100\% \qquad (6)$$

where X represents the capacity in each half cycle during the charge/discharge process, *M* represents the relative molecular mass of $Zn\,(65.38\ g\ mol^{-1})$, ρ represents the zinc density $(7.14\ g\ cm^{-3})$, N_A represents the Avogadro constant $(6.02 \times 10^{23}\ mol^{-1})$, n represents the number of charge transfer of Zn^0 to Zn^{2+}, e represents the electric quantity of a charge $(1.6 \times 10^{-19}C)$ and l represents the thickness of Zn foil $(0.02\ cm)$.

Table S1 Comparison of current additives for zinc ion batteries.

MODIFICATION	**Zn//Zn current density (mA cm^{-2})**	**Zn//Zn capacity (mAh cm^{-2})**	**Zn//Zn Lifespan (h)**	**DOD**	**Ref.**
Acrylamide, ZSO- $Zn(CF_3SO_3)_2$)	30	30	200	-	[13] *Angew. Chem. Int. Ed. 2024*
	10	10	900		
Caffeine polyacrylamide- ZSO	10	10	>350	45%	[14] *Adv.Mater. 2024*
Sodium gluconate-ZSO	5	1	600	80%	[15] *Adv. Funct. Mater. 2024*
Zn@ZnS	1	1	3000	-	[16] *Nano-Micro Lett. 2024*
BR-Zn	5	1	1970	-	[17] *Angew. Chem. Int. Ed. 2024*
	10	3	1100	-	
Tris(hydroxymethyl)aminomethane-ZSO	3	1	2600	-	[18] *Angew. Chem. Int. Ed. 2024*
DTPA-Na -ZSO	2	1	800	-	[19] *Nano-Micro Lett. 2024*
Ce^{3+} and La^{3+}	5	1	700	-	[20] *Energy Environ. Sci. 2021*
1,3-dimethyl-2-imidazolidinone	1	0.5	7220	8.5%	[21] *Energy Environ. Sci. 2024*
Catechol-ZSO	1	1	4000	-	[22] *J. Am. Chem. Soc. 2024*
	10	10	1500	-	
Pluronic F127-$Zn(CF_3SO_3)_2$	1	1	9300	-	[23] *ACS Energy Lett. 2024*
	5	5	3100	-	
$Zn(ClO_4)_2$	1	1	5200	-	[24] *Energy Environ. Mater. 2024*
V_2CT_x	5	2.5	400	-	[25] *Adv. Energy Mater. 2024*
Poly-L-Glutamic Acid- ZSO	2	1	1600	-	[26] *Adv. Funct. Mater. 2024*
N-methyl-2-pyrrolidone-ZnOHF	0.5	6	250	50%	[27] *ACS Energy Lett. 2023*

Cetyltrimethylammonium cations	2	50	300	76.9	[28] *Adv. Energy Mater. 2024*
	4	1	3000	-	
D-mannose& amphipathic sodium lignosulfonate-ZSO	1	0.5	6400	-	[29] *Angew. Chem. Int. Ed. 2024*
Trifluoroacetamide-ZSO	10	1	1100	-	[30] *Energy Environ. Sci. 2024*
	6	3	40	51.24%	
Zn(BBI)$_2$	20	1	700	-	[31] *Adv. Mater. 2023*
	2	2	2800	-	
Acid vitamin-ZSO	10	10	300	34%	[32] *Angew. Chem. Int. Ed. 2024*
THF-Zn(BF$_4$)$_2$	0.25	0.25	2000	-	[33] *Angew. Chem. Int. Ed. 2023*
Theanine-ZSO	5	1	2000	-	[34] *Adv. Funct. Mater. 2024*
	-	46.5	759	80%	
Tributyl phosphate-Zn(TFSI)$_2$	2	1	2100	-	[35] *Energy Environ. Sci., 2024*
Butanone-ZSO	60	60	70	88.2%	[36] *Nat Commun. 2024*
Ammonium persulfate-ZSO	20	8	150	46%	[37] *Adv. Funct. Mater. 2024*
	5	2	4300	-	
Cellulose nanocrystals-ZSO	50	50	982	85.4%	[38] *Angew. Chem. Int. Ed. 2024*
Acetamide-ZSO	-	10	1500	34.1%	[39] *Adv. Funct. Mater. 2024*
	-	25	400	85.3%	
[EMIM]OTF	10	10	500	-	[40] *Adv. Funct. Mater. 2024*
	5	5	900	-	
SBE-β-CD-ZSO	10	10	2000	-	[41] *ACS Nano 2023*
	50	10	170	-	
Bis(2-aminoethyl) amine-ZSO	10	1	2400	-	[42] *Chem Eng J. 2024*

	50	5	212	-	
N, N ’-Methylenebisacrylamide-ZSO	5	5	1000	-	[43] *Energy Storage Mater. 2024*
	10	10	600	-	
Poloxamer-ZSO	5	2.5	2000	-	[44] *ACS Energy Lett. 2024*
4-hydroxybenzaldehyde-ZSO	30	30	120	51.3%	[45] *Energy Storage Mater. 2024*
L-asparagine-ZSO	10	10	240	85.5%	[46] *Adv. Energy Mater. 2023*
Taurine-ZSO	10	5	1000	-	[47] *Energy Storage Mater. 2023*
	20	10	700	-	
Lithium bis(oxalate)borate-ZSO	50	1	1800	-	[48] *Angew. Chem. Int. Ed. 2023*
	100	1	400	-	
LogP- $Zn(CF_3SO_3)_2$	5	5	1600	-	[49] *ACS Nano 2023*
	1	1	4600	-	
DMC, LiNO3- $Zn(OTf)_2$	10	10	1600	-	[50] *Adv. Energy Mater. 2023*
Sodium 3-mercapto-1propanesulfonate-ZSO	1	1	1000	-	[51] *Adv. Funct. Mater. 2024*
Disodium succinate-ZSO	1	1	2200	-	[52] *Adv. Funct. Mater. 2024*
Phenylalanine-ZSO	20	10	500	-	[53] *Nano-Micro Lett. 2024*
	2	2	5250	-	
((Dimethyl(methacryloyloxyethyl) ammonium propane sulfonate-ZSO	0.25	0.25	7000	-	[54] *Angew. Chem. Int. Ed. 2024*
	8	8	135	45.54%	
Butyrolactam-ZSO	10	1	800	-	[55] *Energy Environ. Sci., 2024*
2,3,4,5-tetrahydroxyvaleraldehyde-ZSO	10	1	700	-	[56] *Adv. Funct. Mater. 2024*
Triglycine-ZSO	5	5	400	-	[57] *Adv. Funct. Mater. 2024*

1,2-Ethanedisulfonic acid-ZSO	5	1	1600	-	[58] *Chem Eng J. 2024*
$Zn(Ac)_2$, $Zn(TFA)_2$-$Zn(OTf)_2$	1	1	2400	-	[59] *Energy Environ. Sci., 2024*
Tetrasulfonic acid-ZSO	5	1	2000	-	[60] *Angew. Chem. Int. Ed. 2024*

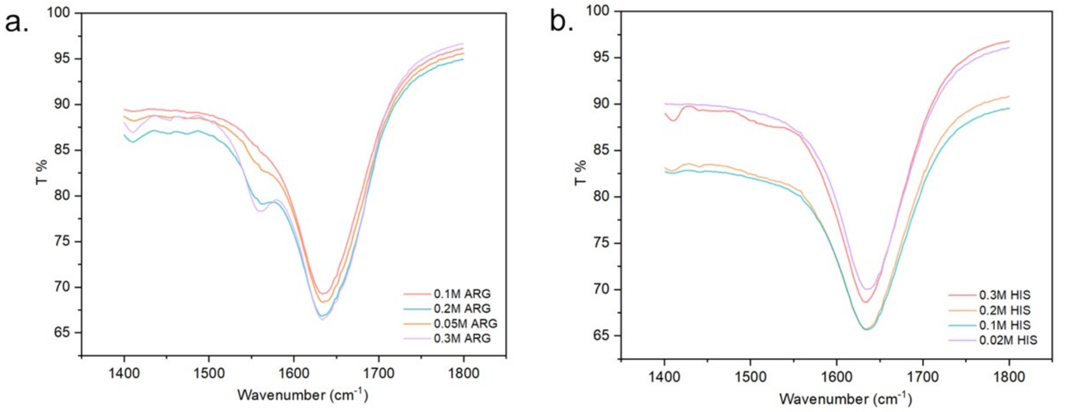

Figure S1 (a) IR spectrum of different concentrations of arginine solution. (b) The IR spectrum of different concentrations of histidine solution.

With the increase of the concentration of arginine, the vibration intensity of –OH bending mode (β(O–H), 1550–1760 cm^{-1}) experiences a stepwise downshift with the increasing arginine concentration, further signifying the existence of arginine–H_2O H−bonds. Same with histidine.

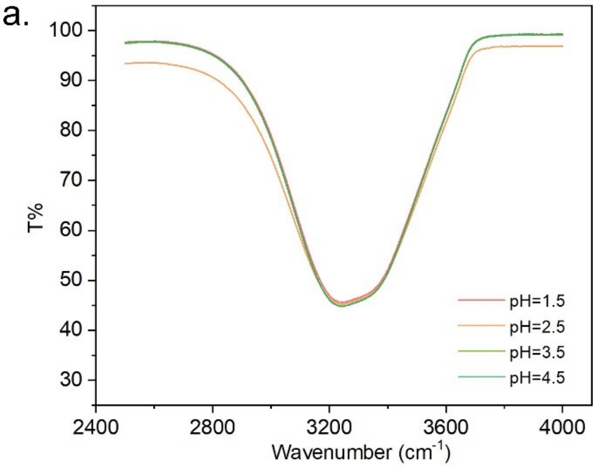

Figure S2 (a) IR spectrum of different pH of solutions when the ZSO concentration is fixed at 1M without additives.

The peak position does not change with the pH value, i.e. the ZSO baseline cannot change the type of H-bond, thus having no effect on adjusting the hydrogen bond net. Also, the ZSO baseline cannot change the type of ion pair, thus having no effect on adjusting the Zn^{2+} solvation structure (contact ion pair).

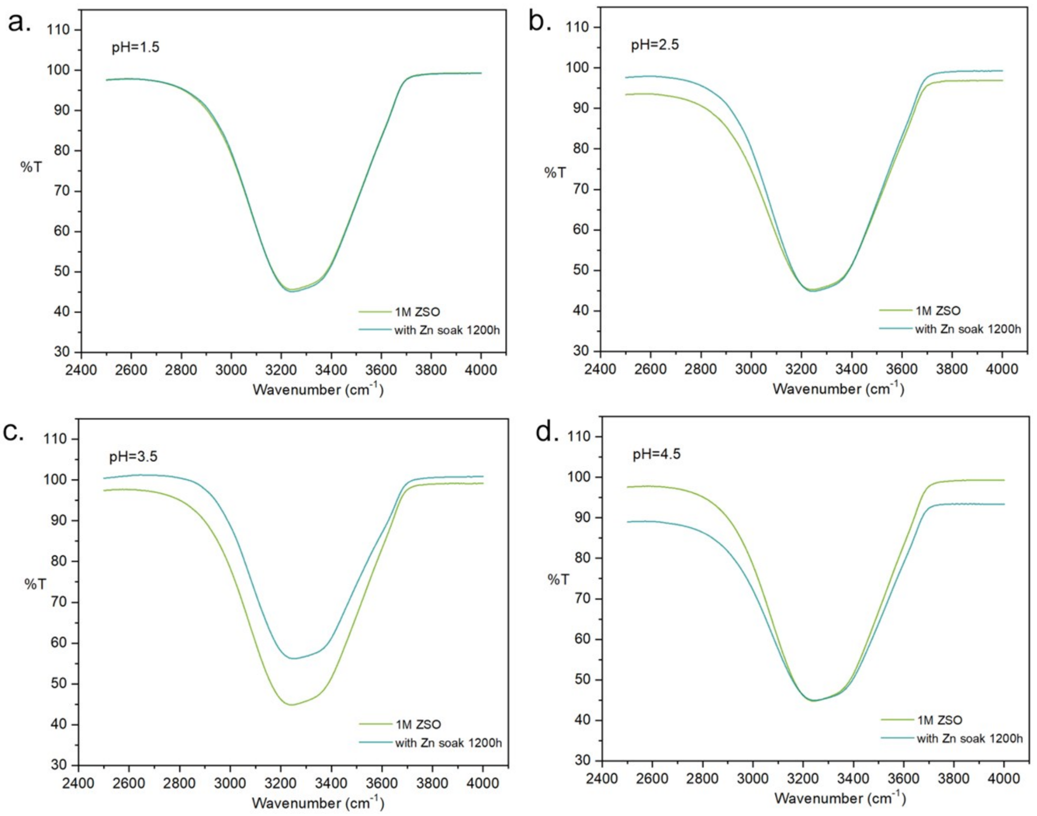

Figure S3 The change in the IR spectrum after Zn soak in the electrolyte without additives addition and different pH values for 1200h.

The peak position does not change with the pH value, i.e. the ZSO baseline cannot change the type of H−bond, thus whatever Zn soak or not, it has no effect on adjusting the hydrogen bond net.

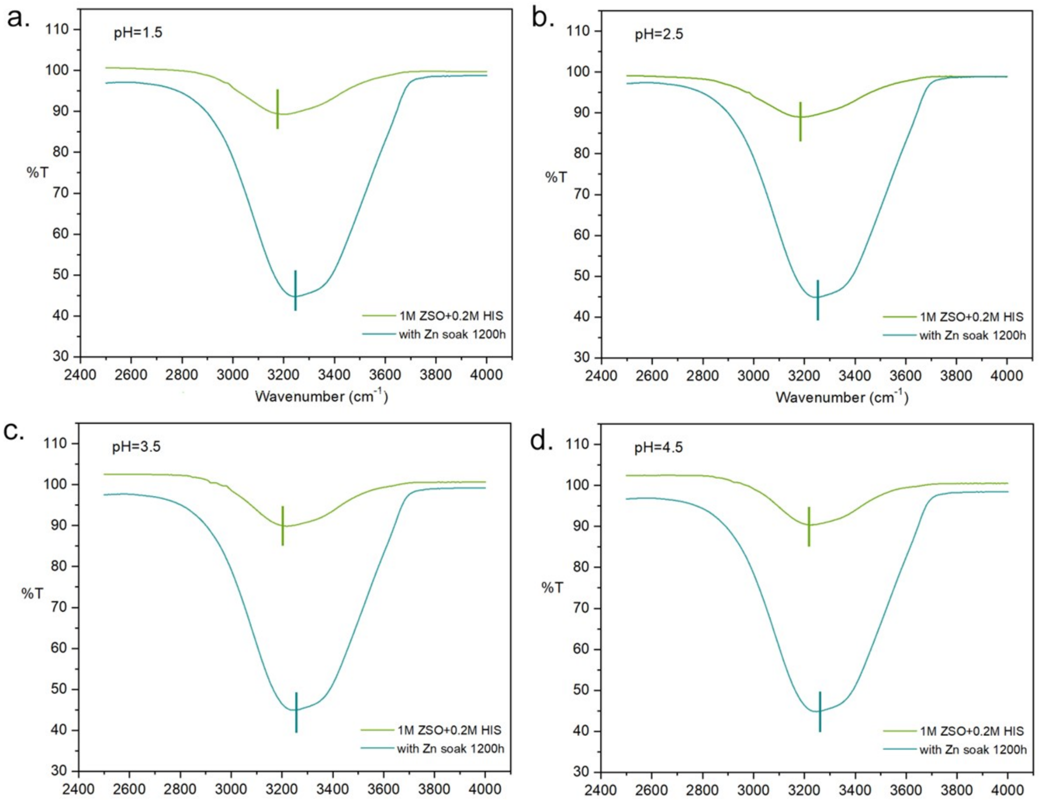

Figure S4 The change in the IR spectrum after Zn soaking in the electrolyte with the addition of 0.2M histidine and different pH values for 1200h.

The peak at 3000-3600 cm^{-1} which shifts to the higher wavenumbers after Zn soaking for 1200h is mainly because of the pH change, the release of H_2 can cause OH^- accumulation, and a more basic electrolyte environment, which can destroy the strength of hydrogen bonds. In the acidic environment, histidine molecules can adsorb protons and when the solution environment becomes basic, it will lose protons. Thus, the buffer property of the histidine will make it to be a hydrogen bond net adjustor to control the change in the pH value.

Intrinsic Molecular Level Properties

Originating from the frontier orbital theory, the electron affinity for reduction corresponds to the electron energy at the lowest unoccupied molecular orbital (LUMO) levels, while the ionization energy for oxidation corresponds to the electron energy at the highest occupied molecular orbital (HOMO) level[61–63].

During zinc ion transfer in the electrolyte, it predominantly forms a six-coordination octahedral structure. As demonstrated by the molecular orbital diagram of the octahedral complex ML_6, the metal valence orbitals interact with ligand σ-orbitals, resulting in M−L σ bonding, where the ligand acts as a σ donor. The t_{2g} orbitals correspond to the HOMO level, and the e_{2g}^* orbitals represent the LUMO level in the newly generated frontier orbitals. The energy gap of the frontier orbitals is influenced by the strength of the ligand as a σ donor. If the ligand exhibits both σ and π characteristics, the σ complex frontier orbitals, including t_{2g} and e_{2g}^* as mentioned earlier, overlap with the HOMO energy level of ligand π-orbitals, leading to the creation of new frontier orbitals (t_{2g} and e_{2g}^*) and new antibonding orbitals (t_{2g}^*). Hence, when selecting ligands for coordination with zinc ions, one of the key factors to consider is the HOMO orbital of the ligand. A higher HOMO orbital of the ligand facilitates electron transfer into the metal, forming a stronger coordination bond.

Additionally, while the HOMO orbital is of significant importance to coordination, the LUMO energy level is also a crucial element in electron transfer. To ensure thermodynamic stability, the electrochemical potential of the electrodes should fall within the electrochemical stability window of the electrolyte, defined as the gap between the oxidation and reduction potentials, i.e., the difference between HOMO and LUMO. The gap between nonbonding and antibonding orbitals controls the hardness of electron transportation, signifying that oxidation resistance increases with a reduction in the energy of HOMO, while the energy of LUMO increases with the strength of the reduction resistance. In other words, a substance with a higher HOMO orbital and lower LUMO orbital is preferable. All the HOMO energy levels of amino acids surpass those of water molecules, indicating faster electron transfer when accompanied by amino acids. Therefore, both in the coordination process and adsorption, zinc atoms preferentially select amino acid additives over water molecules. Figure S5 highlights that serine exhibits the highest HOMO orbital, primarily due to the dispersed HOMO orbital over the entire molecule[61]. Also, arginine and histidine show the lowest HOMO−LUMO gap which indicates the good electron transfer ability. Consequently, serine, histidine, and arginine hold the greatest potential for being applied as an additive to enhance battery performance. Conversely, the HOMO energy level decreases when the orbital is concentrated on electronegative atoms. The HOMO and LUMO orbitals of amino acids encompass the N and O atoms (Figure S6, S7), implying that during adsorption and coordination behavior, N and O atoms act as a 'bridge' connecting additives and zinc atoms. Additional relevant data, including hardness, softness, electronegativity, chemical potential, electrophilicity index, and nucleophilicity index, can be found in Table S2.

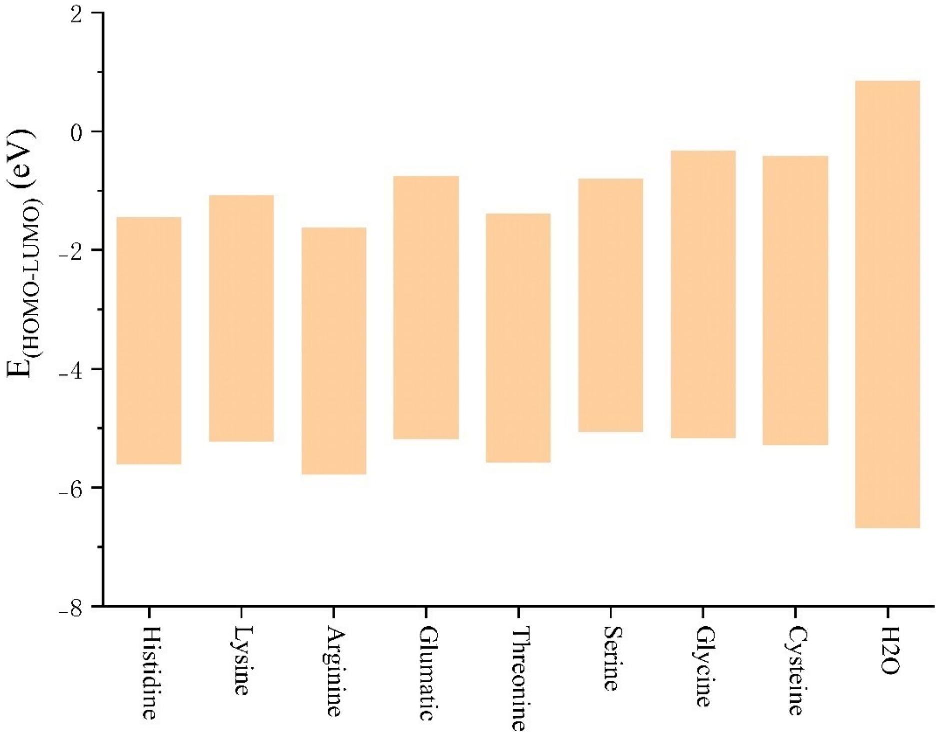

Figure S5. The energy value of HOMO and LUMO orbitals of amino acid molecules and the corresponding energy gaps.

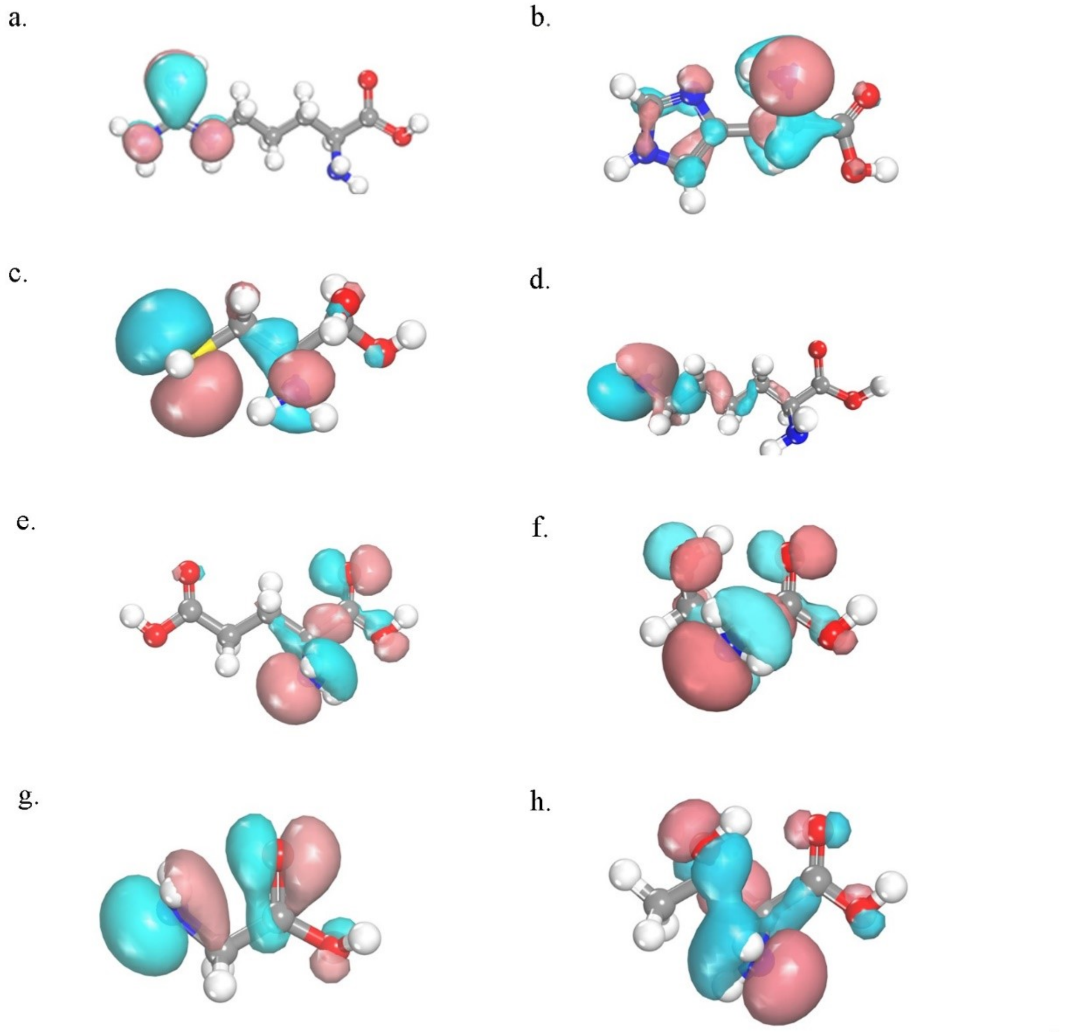

Figure S6. The energy value of HOMO orbitals of amino acid molecules and the corresponding energy gaps. The molecular electrostatic potential mapping of (a) arginine, (b) histidine, (c) cysteine, (d) lysine, (e) glutamic acid, (f) serine, (g) glycine, and (h) threonine.

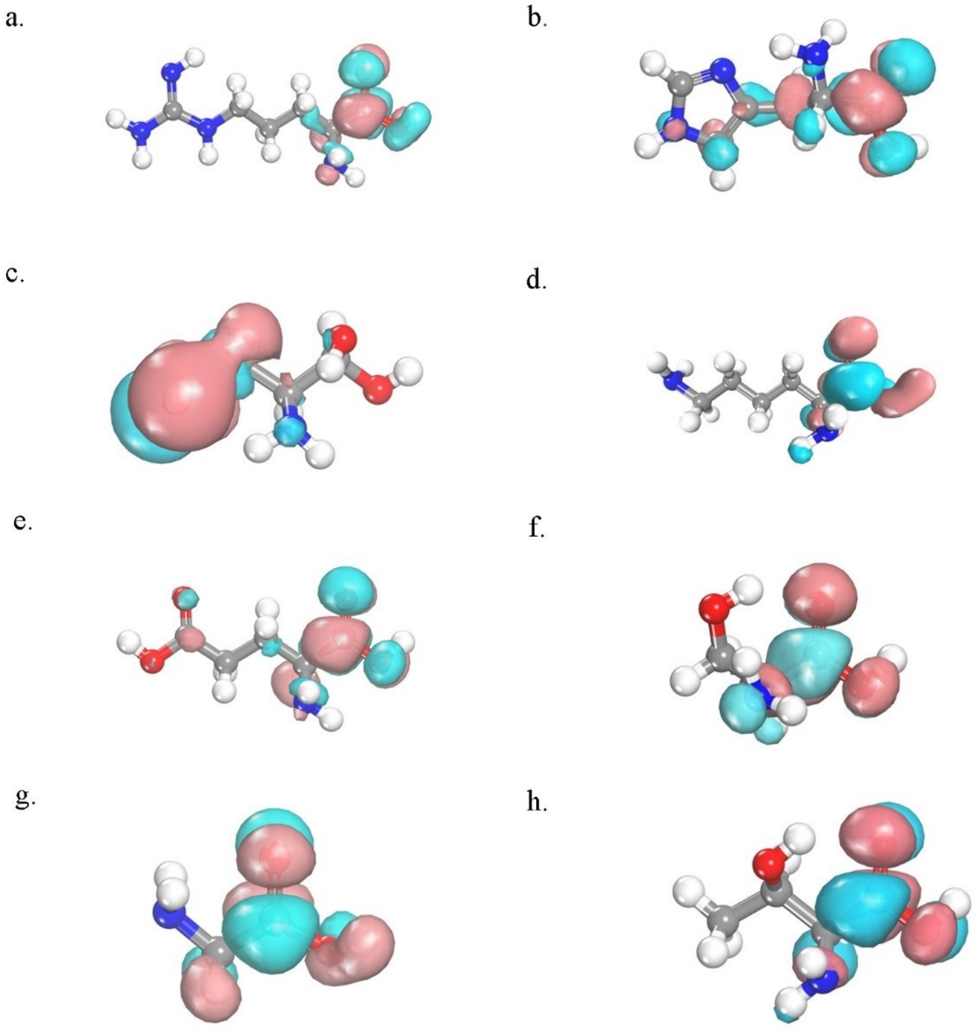

Figure S7. The LUMO orbitals isosurface of (a) arginine, (b) histidine, (c) cysteine, (d) lysine, (e) glutamic acid, (f) serine, (g) glycine, and (h) threonine.

Table S2 Corresponding data of additives properties.

Type of amino acids	Electron affinity	Ionization potential	Global hardness	Electronegative index	Chemical potential	Electrophilicity index	Global softness	Nucleophilicity index
Histidine	1.450	5.613	2.082	3.532	3.532	12.980	0.480	0.077
Cysteine	0.417	5.282	2.433	2.850	2.850	9.876	0.411	0.101
Lysine	1.080	5.230	2.075	3.155	3.155	10.327	0.482	0.097
Arginine	1.617	5.778	2.081	3.698	3.698	14.222	0.481	0.070
Glycine	0.325	5.163	2.419	2.744	2.744	9.107	0.413	0.110
Threonine	1.385	5.579	2.097	3.482	3.482	12.709	0.477	0.079
Glutamic acid	0.754	5.187	2.217	2.971	2.971	9.779	0.451	0.102
Serine	0.800	5.060	2.130	2.930	2.930	9.143	0.469	0.109

Solvation Energy Calculation

In this study, we aimed to investigate the impact of adding amino acids on solvation structures and subsequently, their influence on the deposition behavior of zinc ions. To achieve this, we employed MD simulations to analyze different solvation sheaths and compare the solvation energies in the presence of various amino acid additives at concentrations of 0.1M, 0.15M, and 0.2M in both 1M ZSO and 5M ZSO solutions. Under mildly acidic conditions, zinc ions exist as $(Zn(OH_2)_6)^{2+}$ due to the formation of a solvation shell resulting from hydrolysis processes. However, the desolvation of zinc ions can lead to undesirable HER when the zinc anode comes into contact with water from the solvation sheath. To mitigate this, one approach involves replacing some of the water molecules in the solvation sheath with other substances, reducing the amount of water transferred to the anode surface. This reduction in HER occurrences can help minimize the formation of dendrites, which is desirable.

Solvation Energy Calculation in 1M ZSO

Even though the solvation structures $(Zn(OH_2)_6)^{2+}$ have the same composition across different electrolyte conditions, the solvation energies vary with different additive additions. The highest solvation energy locations are found in lysine, according to Figure S8a, whereas the lowest solvation energies are found in arginine. Considering the configuration of $Zn(H_2O)_5$(amino acids) with the presence of amino acids, the solvation energy rank list in 1M ZSO exhibits the following order: serine, arginine, histidine, glutamic acid, cysteine, lysine, threonine, and glycine, with comparable values observed for cysteine and lysine (Figure S8b, e). The solution models under specific conditions of 1M ZSO and amino acids at varying concentrations (0.1M, 0.15M, 0.2M) with polar-charged and polar-uncharged amino acids participated in are depicted in Figure S9, S10, and Figure S11, S12 present the pertinent solvation structures.

The investigation focuses on the solvation energy analysis of polar-charged amino acids, with particular attention to arginine, which exhibits the most negative solvation energy, suggesting its suitability as an additive. The presence of arginine in the solvation sheath hinders the deposition of zinc ions, resulting in a smoother zinc anode surface, and histidine follows as the second-best option (Figure S8b). Similarly, glutamic acid ranks third, and 0.1M concentration proves to have the highest solvation energy (−500.36 kcal/mol). Lysine is ranked last, with an optimal additive concentration of 0.2M, resulting in a solvation energy of −478.50 kcal/mol. Figure S8b reveals that, with the exception of serine, polar-charged amino acids generally exhibit higher solvation energies compared to polar uncharged amino acids. Moreover, the solvation energy values for systems containing additive molecules are consistently larger than those comprising only water and zinc ions.

Within the categorization of polar-uncharged amino acids, serine stands out with the remarkably highest solvation energy among all types of additives, from Figure S8e. At a concentration of 0.2M, it exhibits the most elevated solvation energy, leading to the highest overpotential for deposition, quantified at −2093.15 kcal/mol. For alternative concentrations, serine demonstrates solvation energies of −2059.97 kcal/mol for 0.15M and −2066.71 kcal/mol for 0.1M. However, excessive solvation can lead to high resistance in the desolvation process, and it is difficult for zinc ions to deposit on the anode surface. As shown in Figure S8b cystine secures the second position with the classification of polar-uncharged amino acids, and the most favorable concentration yielding the highest solvation energy is 0.1M, reaching −484.26 kcal/mol. Threonine occupies the third position, with nearly similar solvation energies observed for concentrations of 0.1M, 0.15M, and 0.2M. Glycine ranks last, displaying comparable solvation energies at concentrations of 0.1M (−401.27 kcal/mol) and 0.15M (−397.13 kcal/mol), which are both higher than the solvation energy observed at 0.2M concentration. Notably, all solvation energy values involving additive molecules surpass those of $(Zn(OH_2)_6)^{2+}$.

Solvation Energy Calculation in 5M ZSO

Despite the identical composition of solvation structures $(Zn(OH_2)_6)^{2+}$ in diverse electrolyte environments, their respective solvation energies vary significantly, which can be seen in Figure S8c. In essence, the presence of different additives leads to distinct solvation energy outcomes for $(Zn(OH_2)_6)^{2+}$. Figure S8d illustrates that glycine at a concentration of 0.1M exhibits the lowest solvation energy, whereas serine at 0.2M demonstrates the highest solvation energy. The solution models under particular circumstances of 5M ZSO and amino acids at different concentrations (0.1M, 0.15M, and 0.2M) are shown in Figures S13, and S14. Figures S15 and S16 exhibit the appropriate solvation structures. The rank list of solvation energy in 5M with the presence of amino acids is as follows: serine, arginine, histidine, glutamic acid, cysteine, lysine, threonine, and glycine, with histidine, cysteine, and glutamic acid exhibiting comparable values.

The solvation energy analysis of polar charged amino acids in 5M electrolyte reveals that arginine possesses the most negative solvation energies, indicating its suitability as an additive for this electrolyte (Figure S8d). When zinc ions separate from the solvation sheath, the difficulty of their deposition contributes to the attainment of a smoother zinc anode surface. Optimal results are achieved with a 0.2M concentration of arginine additive, yielding a solvation energy of -629.49 kcal/mol. Histidine secures the second position, with a preferred additive concentration of 0.15M, resulting in a solvation energy of -550.90 kcal/mol. In the third position, glutamic acid exhibits its highest solvation energy at a concentration of 0.2M additive (-548.41 kcal/mol). Lysine is considered the least effective, with an optimal additive concentration of 0.1M and a solvation energy of -506.38 kcal/mol.

Remarkably, among all types of additives including polar-uncharged amino acids, serine displays the highest solvation energy (Figure S8f). Notably, it achieves the highest solvation energy at 0.15M concentration, leading to the greatest overpotential for deposition (-2126.87 kcal/mol). For other concentrations, serine exhibits solvation energies of -2093.48 kcal/mol at 0.2M and -2104.40 kcal/mol at 0.1M. Cystine ranks second of all polar-uncharged amino acids, and its optimal concentration for the maximum solvation energy is 0.15M, corresponding to -545.57 kcal/mol (Figure S8d). Threonine occupies the third position, with comparable solvation energies observed at 0.1M and 0.15M concentrations, where the highest solvation energy is -469.01 kcal/mol. Glycine, the final compound, demonstrates similar solvation energies at additive concentrations of 0.1M and 0.2M, both smaller than that observed at 0.2M concentration (-367.49 kcal/mol). Additionally, the solvation energies of all solvation sheaths containing polar-uncharged amino acid molecules surpass that of $(Zn(OH_2)_6)^{2+}$.

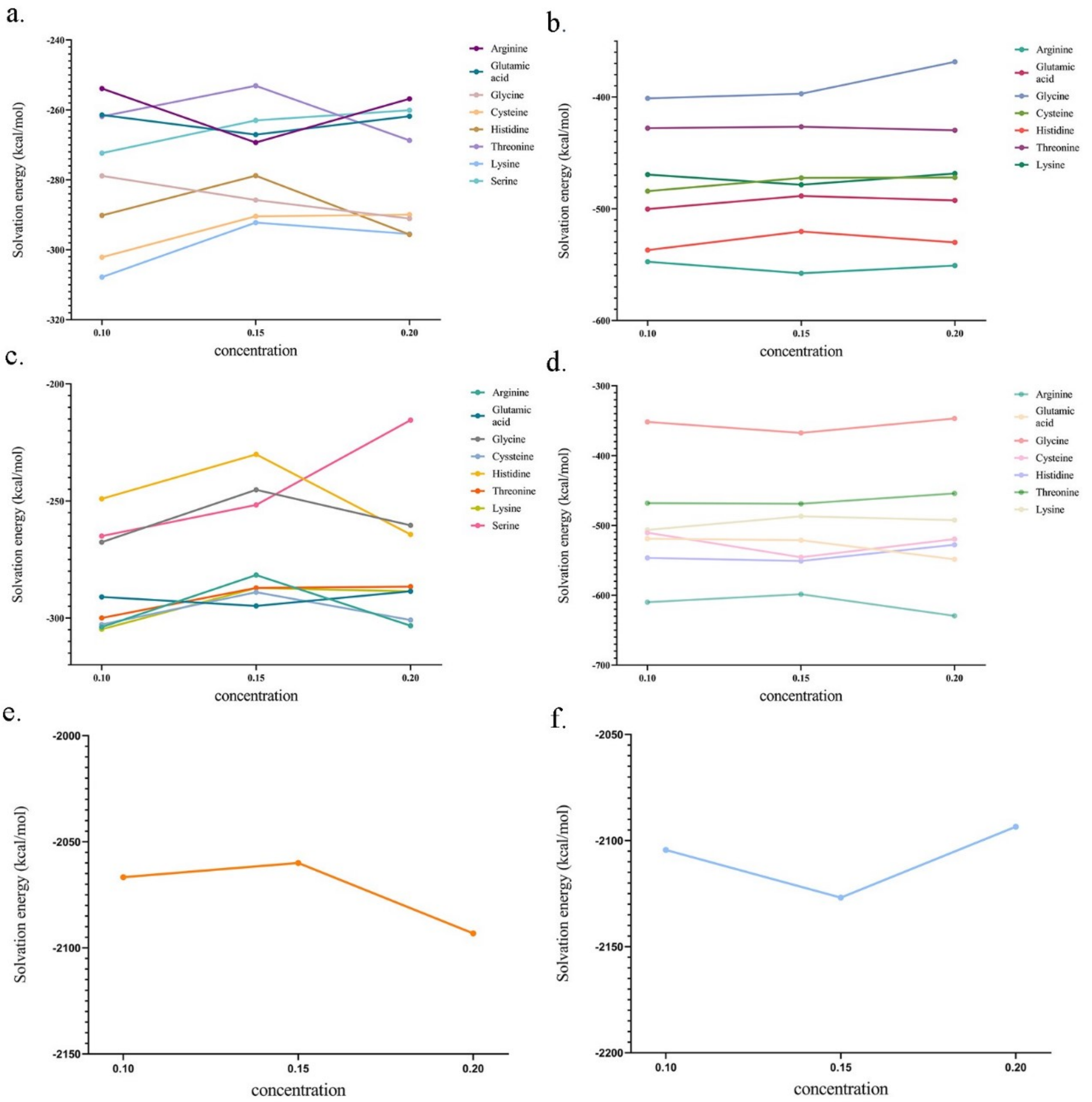

Figure S8 (a) The solvation energy of zinc ion separated from the solvation structure of $(Zn(OH_2)_6)^{2+}$ in 1M ZSO. (b) The solvation energy of the zinc ion separated from the solvation structure which contained amino acids in 1M ZSO. (c) The solvation energy of zinc ion separated from the solvation structure of $(Zn(OH_2)_6)^{2+}$ in 5M ZSO. (d) The solvation energy of the zinc ion separated from the solvation structure which contained amino acids in 5M ZSO. (e) The solvation energy of the zinc ion separated from the solvation structure which contained serine in 1M ZSO. (f) The solvation energy of the zinc ion separated from the solvation structure which contained serine in 5M ZSO.

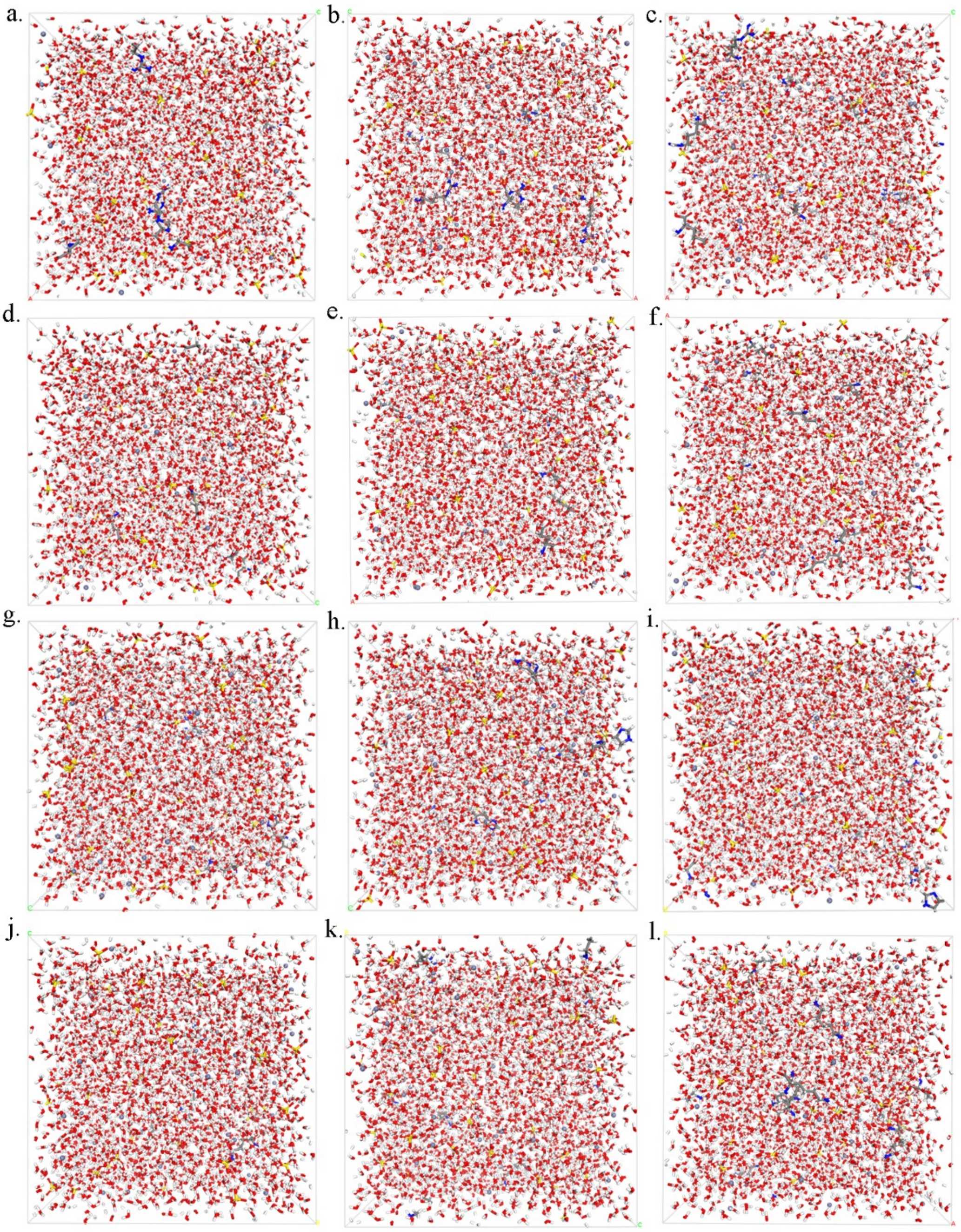

Figure S9. The solution model with the addition of polar charged amino acids with distinctive concentrations (a) 0.1M arginine, (b) 0.15M arginine, (c) 0.2M arginine (d) 0.1M glutamic acid, (e) 0.15M glutamic acid, (f) 0.2M glutamic acid, (g) 0.1M histidine, (h) 0.15M histidine, (i) 0.2M histidine, (j) 0.1M lysine, (k) 0.15M lysine, (l) 0.2M lysine in 1M using MD simulation.

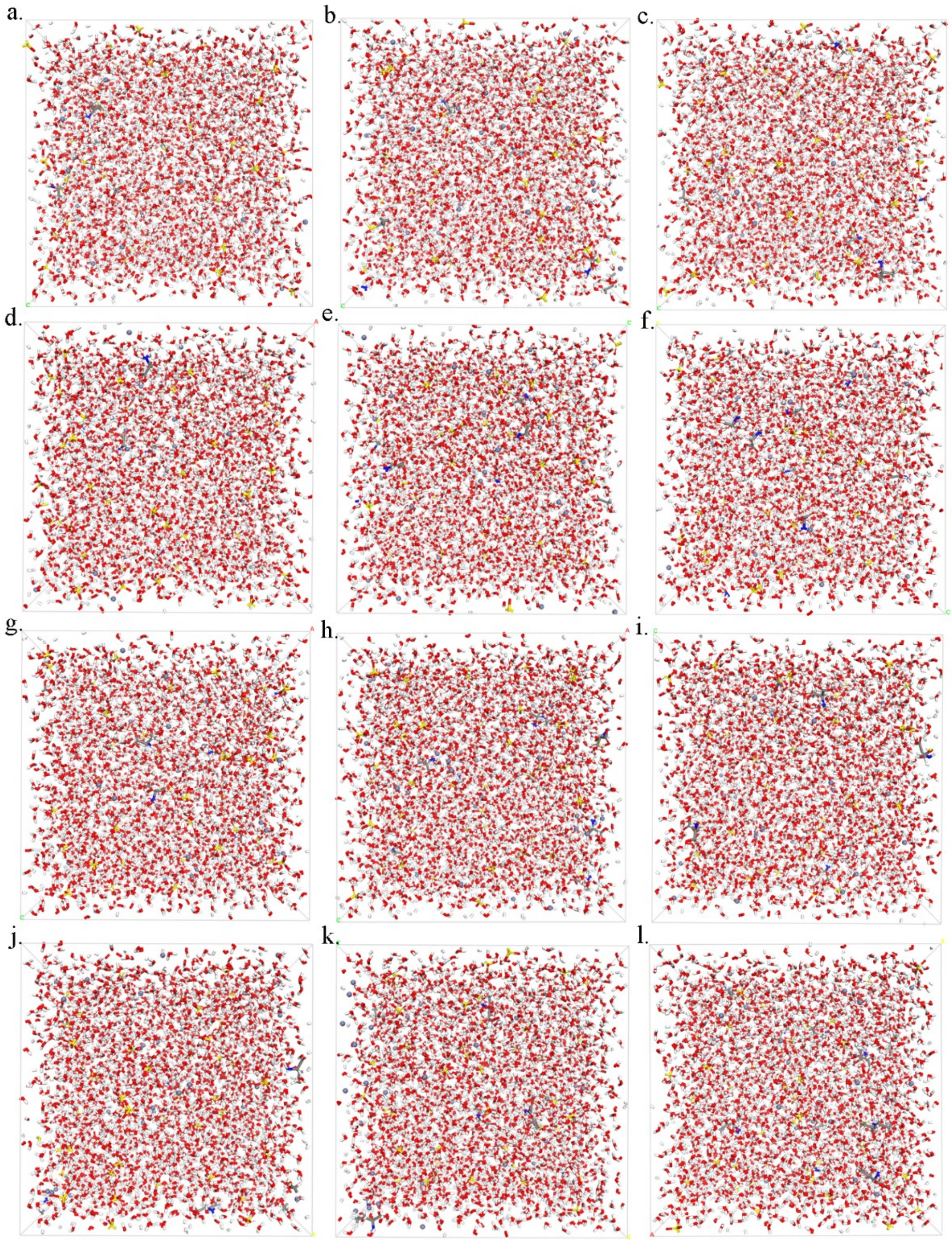

Figure S10. The solution model with the addition of polar uncharged amino acids with distinctive concentrations (a) 0.1M cysteine, (b) 0.15M cysteine, (c) 0.2M cysteine (d) 0.1M glycine, (e) 0.15M glycine, (f) 0.2M glycine, (g) 0.1M serine, (h) 0.15M serine, (i) 0.2M serine, (j) 0.1M threonine, (k) 0.15M threonine, (l) 0.2M threonine in 1M using MD simulation.

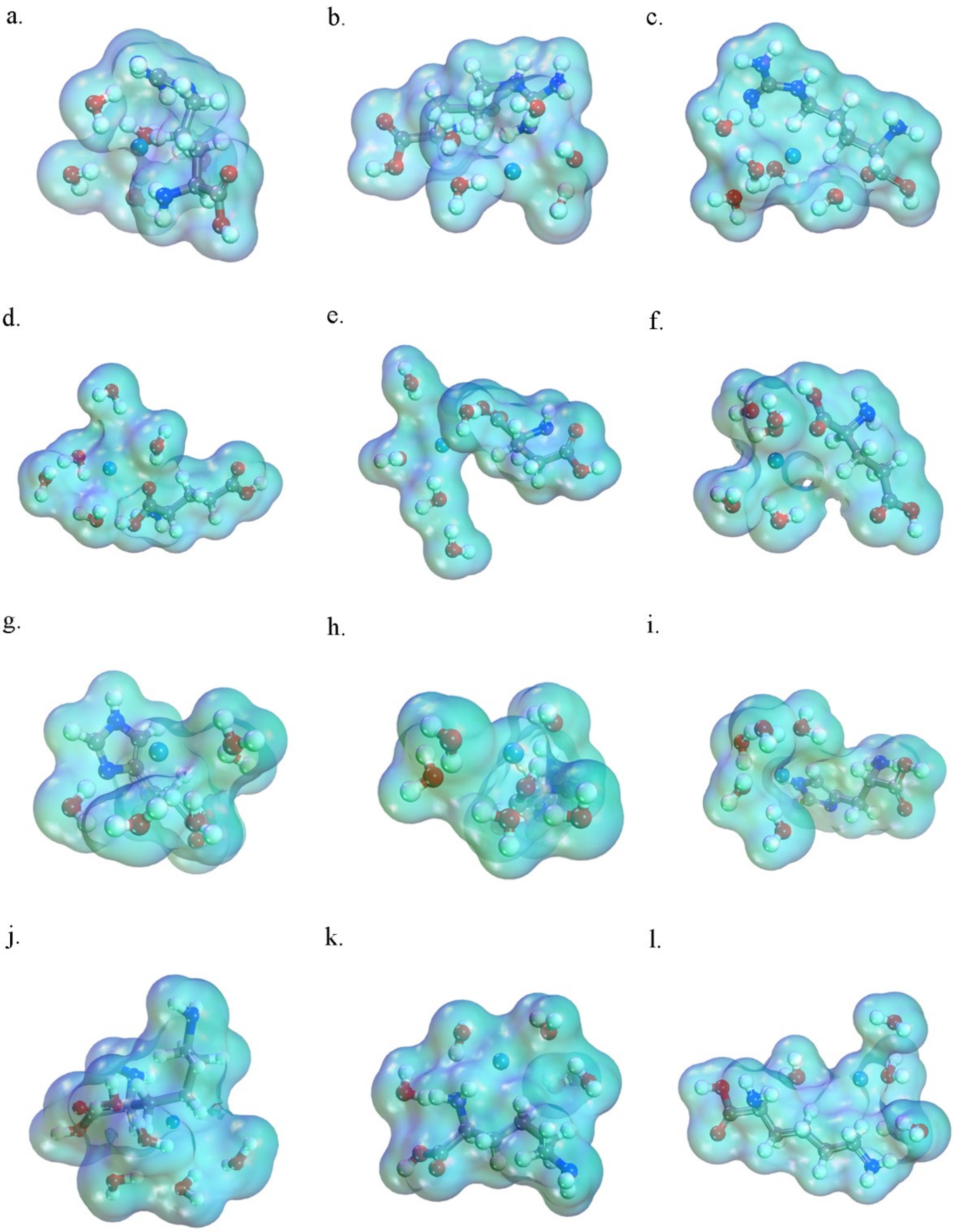

Figure S11. The solvation structure separated from the electrolyte with the addition of polar charged amino acids with distinctive concentrations (a) 0.1M arginine, (b) 0.15M arginine, (c) 0.2M arginine (d) 0.1M glutamic acid, (e) 0.15M glutamic acid, (f) 0.2M glutamic acid, (g) 0.1M histidine, (h) 0.15M histidine, (i) 0.2M histidine, (j) 0.1M lysine, (k) 0.15M lysine, (l) 0.2M lysine in 1M using MD simulation.

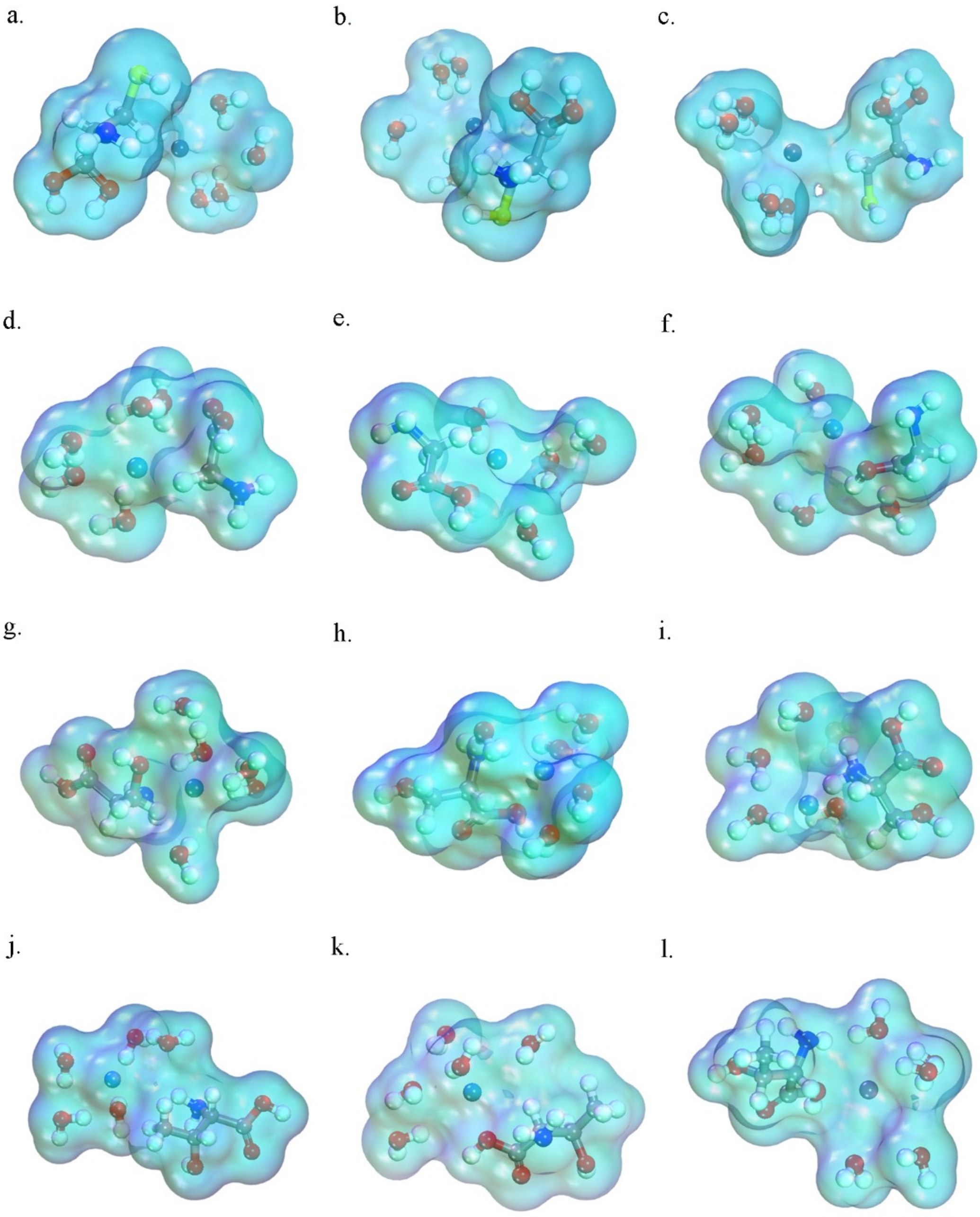

Figure S12. The solvation structure separated from the electrolyte with the addition of polar uncharged amino acids with distinctive concentrations (a) 0.1M cysteine, (b) 0.15M cysteine, (c) 0.2M cysteine, (d) 0.1M glycine, (e) 0.15M glycine, (f) 0.2M glycine, (g) 0.1M serine, (h) 0.15M serine, (i) 0.2M serine, (j) 0.1M threonine, (k) 0.15M threonine, (l) 0.2M threonine in 1M using MD simulation.

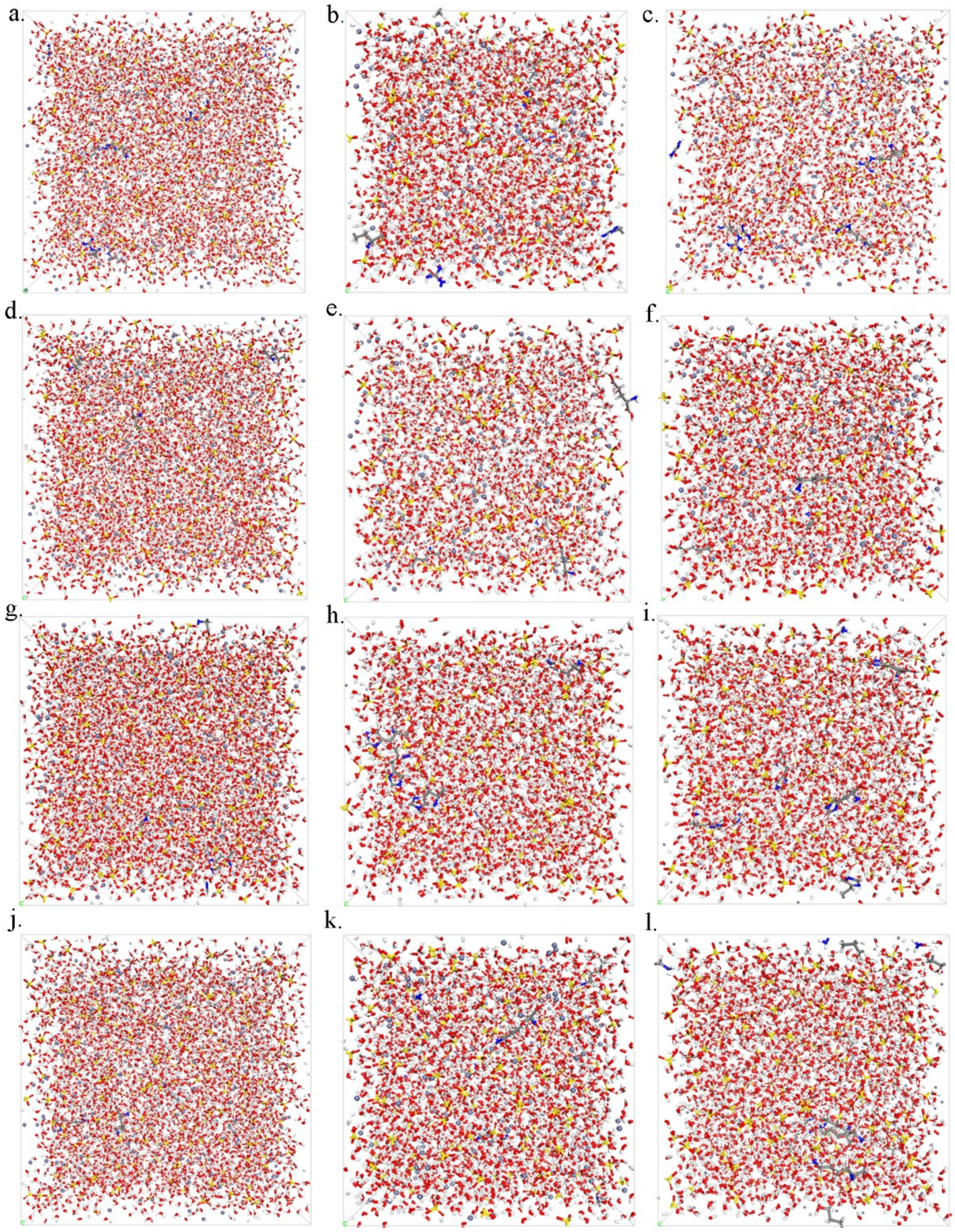

Figure S13. The solution model with the addition of polar charged amino acids with distinctive concentrations (a) 0.1M arginine, (b) 0.15M arginine, (c) 0.2M arginine (d) 0.1M glutamic acid, (e) 0.15M glutamic acid, (f) 0.2M glutamic acid, (g) 0.1M histidine, (h) 0.15M histidine, (i) 0.2M histidine, (j) 0.1M lysine, (k) 0.15M lysine, (l) 0.2M lysine in 5M using MD simulation.

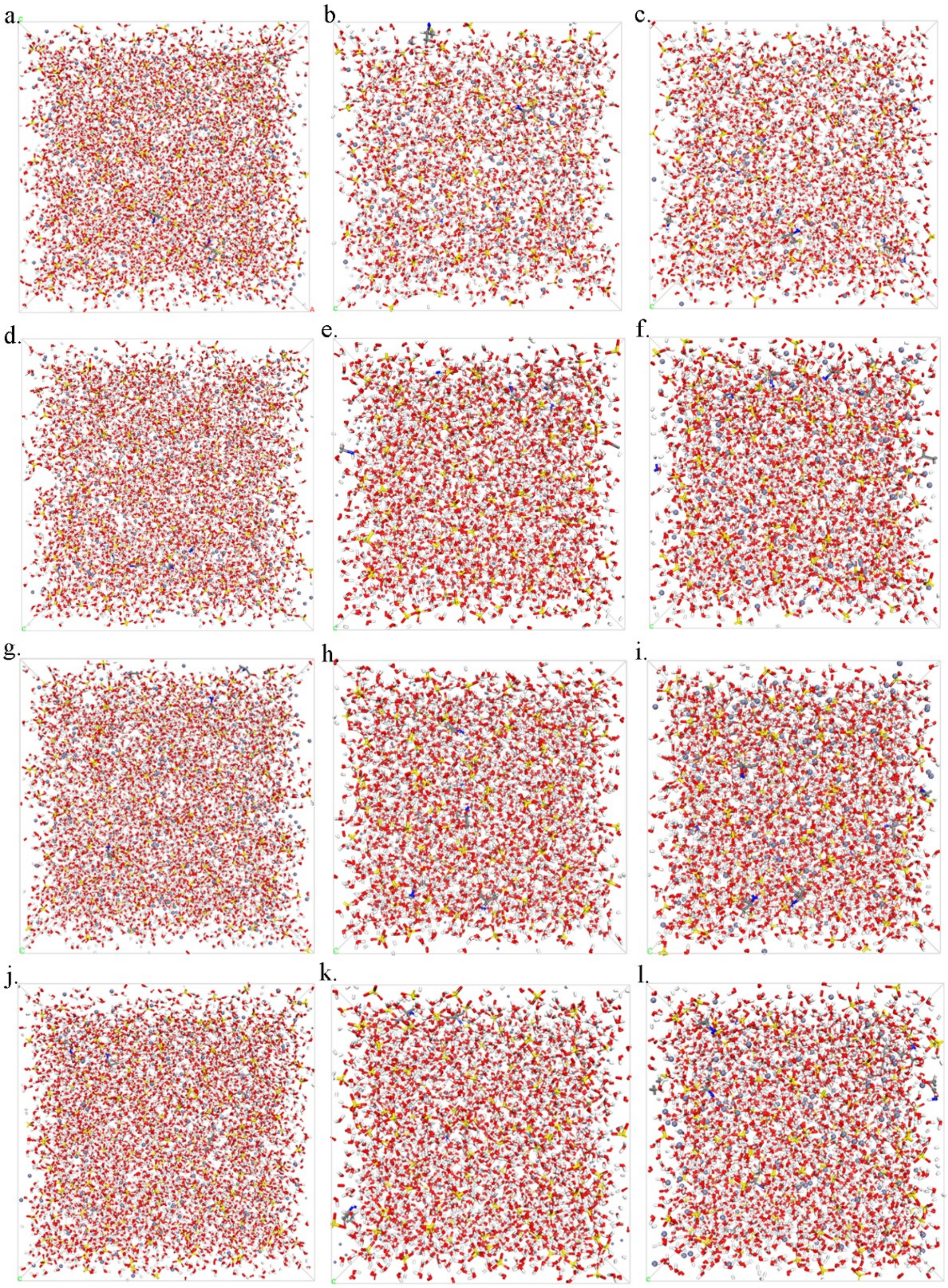

Figure S14. The solution model with the addition of polar uncharged amino acids with distinctive concentrations (a) 0.1M cysteine, (b) 0.15M cysteine, (c) 0.2M cysteine (d) 0.1M glycine, (e) 0.15M glycine, (f) 0.2M glycine, (g) 0.1M serine, (h) 0.15M serine, (i) 0.2M serine, (j) 0.1M threonine, (k) 0.15M threonine, (l) 0.2M threonine in 5M using MD simulation.

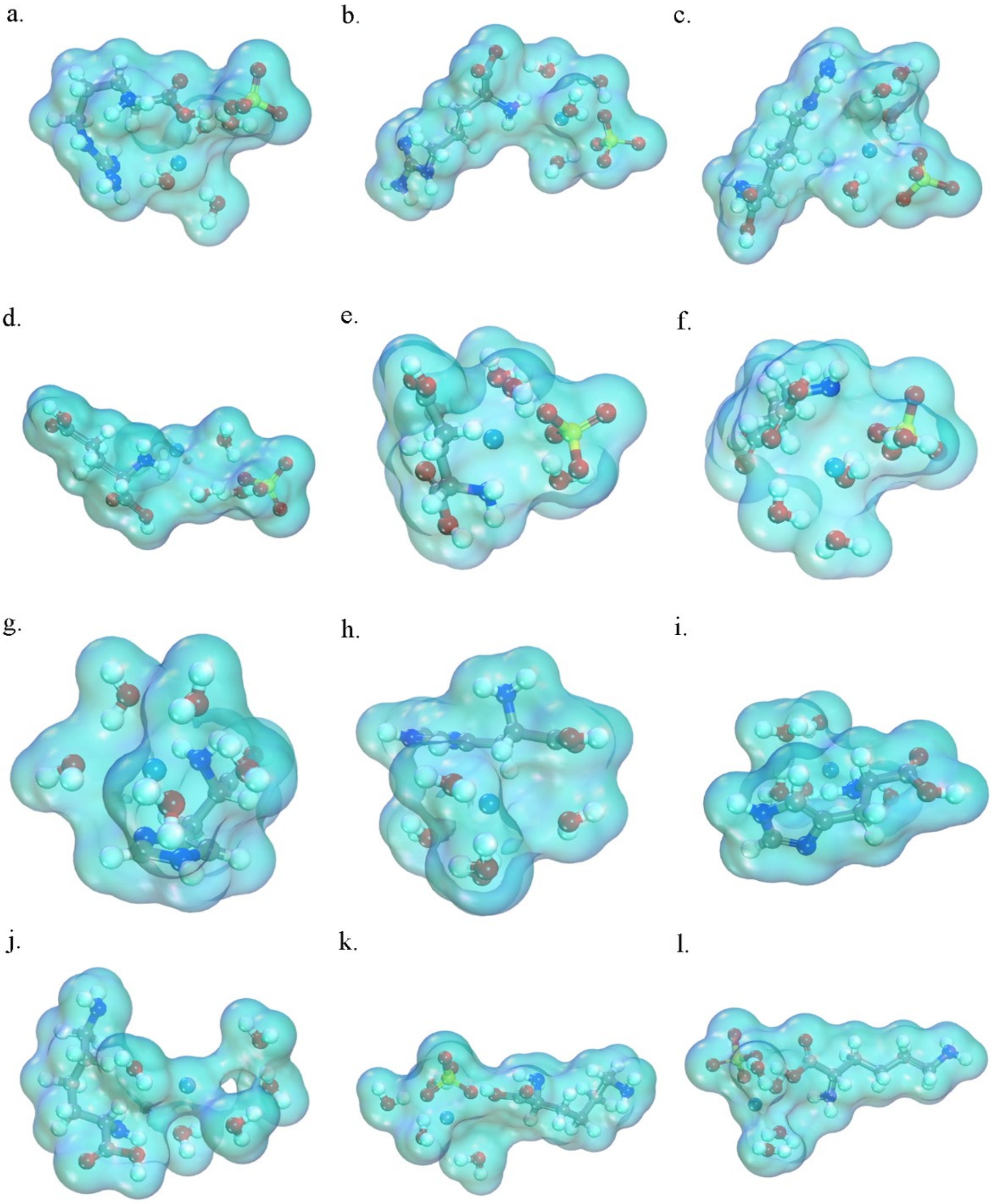

Figure S15. The solvation structure separated from the electrolyte with the addition of polar charged amino acids with distinctive concentrations (a) 0.1M arginine, (b) 0.15M arginine, (c) 0.2M arginine (d) 0.1M glutamic acid, (e) 0.15M glutamic acid, (f) 0.2M glutamic acid, (g) 0.1M histidine, (h) 0.15M histidine, (i) 0.2M histidine, (j) 0.1M lysine, (k) 0.15M lysine, (l) 0.2M lysine in 5M using MD simulation.

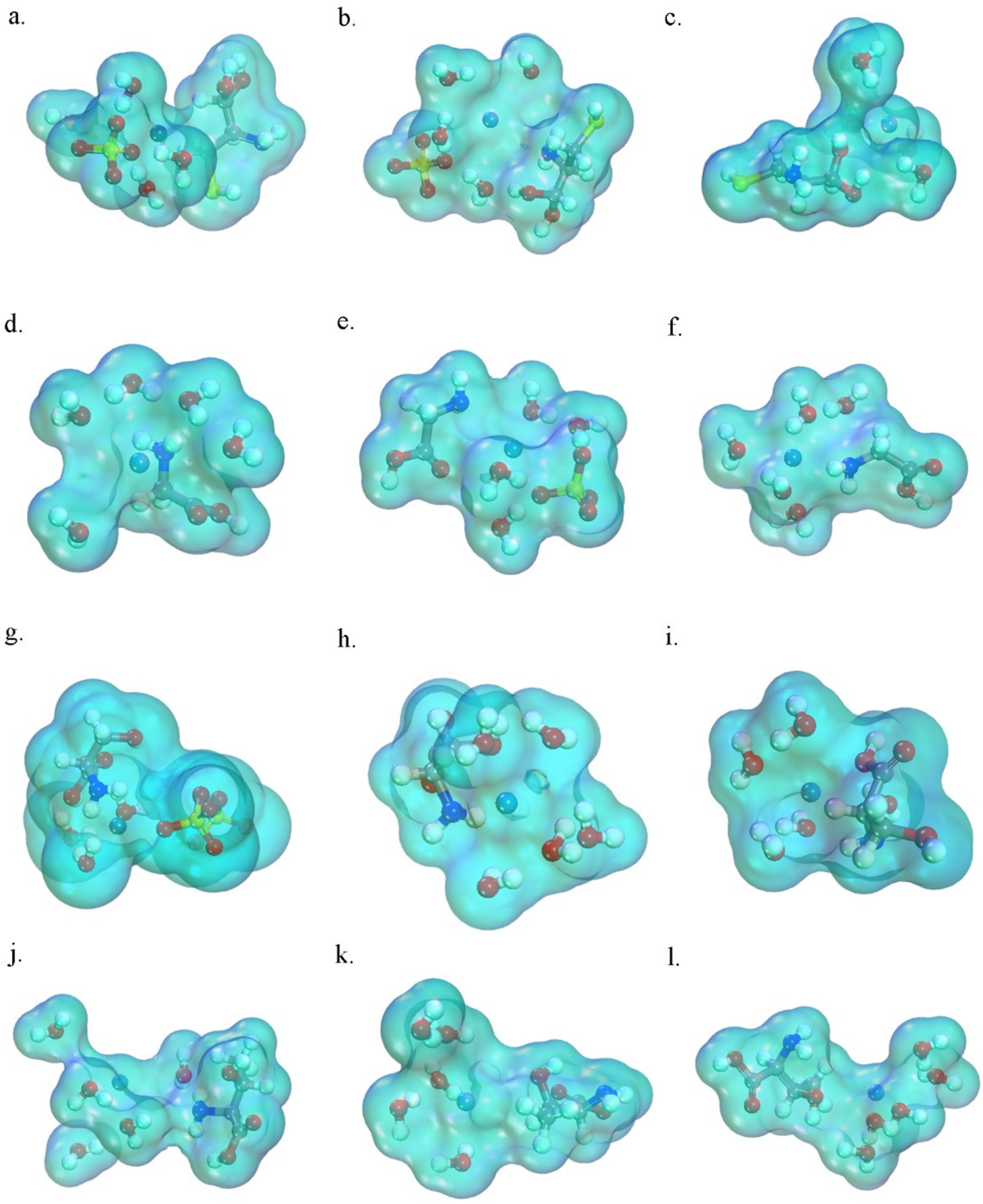

Figure S16. The solvation structure separated from the electrolyte with the addition of polar uncharged amino acids with distinctive concentrations (a) 0.1M cysteine, (b) 0.15M cysteine, (c) 0.2M cysteine (d) 0.1M glycine, (e) 0.15M glycine, (f) 0.2M glycine, (g) 0.1M serine, (h) 0.15M serine, (i) 0.2M serine, (j) 0.1M threonine, (k) 0.15M threonine, (l) 0.2M threonine in 5M using MD simulation

The Zn-Amino Acid Binding Energy Calculation

The evaluation of solvation energy encompasses the entire solvation sheath, accounting for factors such as steric hindrance of additive molecules, interactions between water molecules and additives, water-water interactions, and additive-additive interactions. The binding energy analysis between zinc ions and amino acids effectively eliminates confounding factors and provides specific insights into the influence of additives on zinc ions. Similarly, the binding energy rank list in 1M follows a sequence from the most negative to the most positive: serine, arginine, histidine, glutamic acid, cysteine, lysine, threonine, and glycine. Notably, there is a significant correlation between the data on binding energies and solvation energies. The two sets of data exhibit identical ranking orders, whether in 1M or 5M conditions.

The Zn-Amino Acid Binding Energy Calculation in 1M ZSO

Under the addition of polar-charged amino acids, Zn-amino acid binding energy calculation in 1M reveals that Zn-arginine exhibits the highest absolute value, with 0.15M concentration yielding the optimal binding energy of −443.57 kcal/mol (Figure S17c). Following this, the binding energy between histidine and zinc ion is observed, with similar values obtained for additive concentrations of 0.1M and 0.2M, yielding −384.71 kcal/mol and −383.30 kcal/mol, respectively. The third position is occupied by the binding energy between zinc ion and glutamic acid, with 0.15M additive concentration producing the highest binding energy (−370.49 kcal/mol). Lysine ranks fourth, with the highest binding energy calculated at −334.37 kcal/mol for an additive concentration of 0.15M.

In the case of polar-uncharged amino acids, serine exhibits the largest binding energy, with 0.1M concentration leading to the highest value of −1963.81 kcal/mol (Figure S17a). Consequently, based on the binding energy calculation, serine is the most optimal choice. Cysteine follows in second place, with the highest binding energy observed at −354.98 kcal/mol (Figure S17c). Threonine secures the third position, with the highest binding energy of −307.56 kcal/mol at 0.1M concentration. Among all amino acids, glycine displays the lowest binding energy, with the highest value obtained at 0.15M concentration (−225.90 kcal/mol).

The Zn-Amino Acid Binding Energy Calculation in 5M ZSO

Similarly, the binding energy rank list in 5M follows the sequence from the most negative to the most positive: serine, arginine, histidine, glutamic acid, cysteine, lysine, threonine, and glycine, where cysteine and glutamic acid also demonstrate comparable values. Notably, substantial correlations are observed between the data on binding energies and solvation energies and the two sets of data exhibit an identical ranking order, regardless of the concentration (1M or 5M).

In the analysis of polar-charged amino acids and zinc ions, Zn-arginine exhibits the highest binding affinity, with 0.2M concentration yielding the highest absolute value of binding energy (−462.78 kcal/mol) (Figure S17d). For histidine, the binding energies at additive concentrations of 0.1M and 0.2M are approximately similar, measuring −384.96 kcal/mol and −383.92 kcal/mol, respectively. The third position is occupied by the binding energy between zinc ion and glutamic acid, with 0.2M concentration producing the greatest binding energy (−370.85 kcal/mol). Lysine ranks fourth, with the highest binding energy calculated at −347.25 kcal/mol for an additive concentration of 0.2M.

Among polar-uncharged amino acids, serine demonstrates the highest binding energy, with a value of −1976.00 kcal/mol at 0.1M concentration (Figure S17b). Therefore, serine emerges as the optimal choice when considering the binding energy estimate. For cysteine, the highest binding energy is recorded at −368.38 kcal/mol at 0.15M (Figure S17d). Threonine secures the third position, exhibiting the greatest binding energy of −324.10 kcal/mol at 0.1M concentration. Glycine, characterized by the lowest binding energy among all amino acids, displays its highest binding energy at 0.2M concentration (−228.28 kcal/mol).

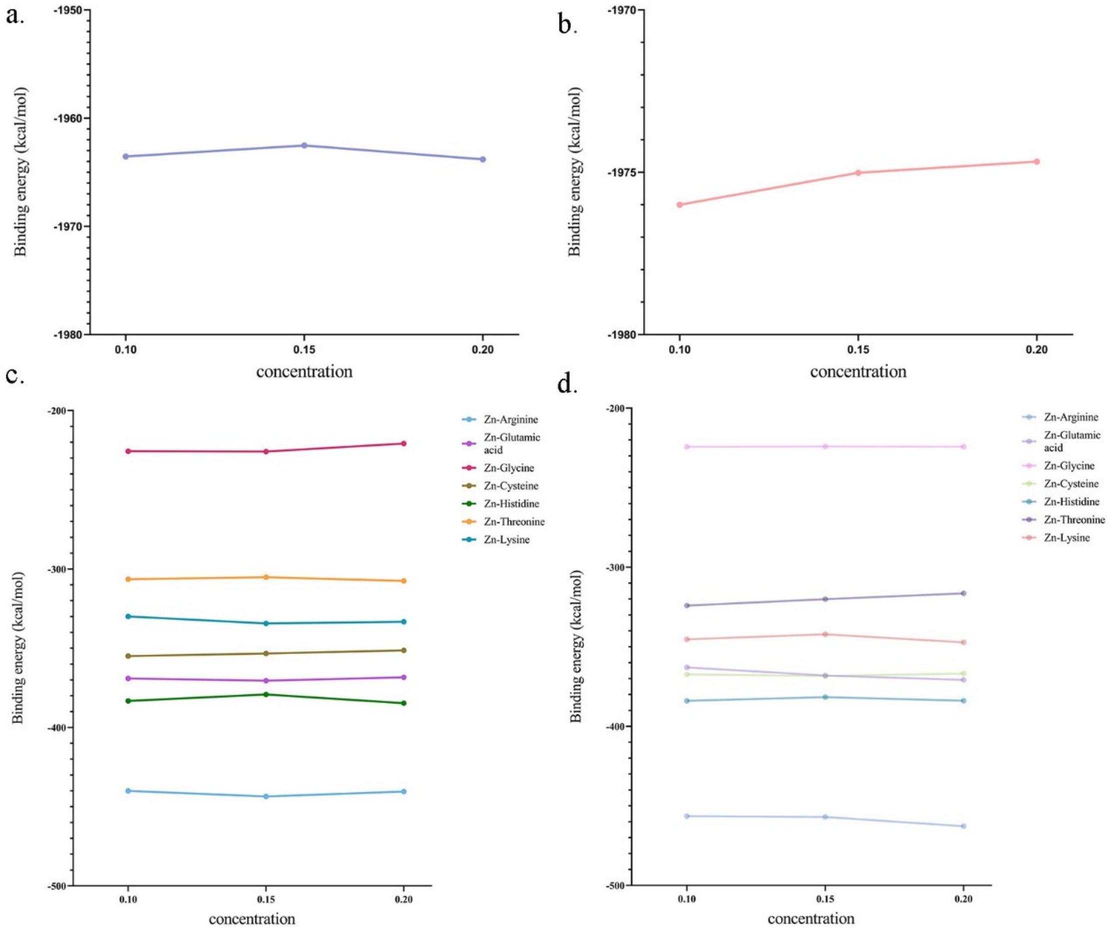

Figure S17. The binding energy between zinc ion and serine in the solvation structure with the environment of (a) 1M ZSO and (b) 5M ZSO. The binding energy between zinc ions and amino acids in the solvation structures with the environment of (c) 1M ZSO (d) 5M ZSO, using MD simulation.

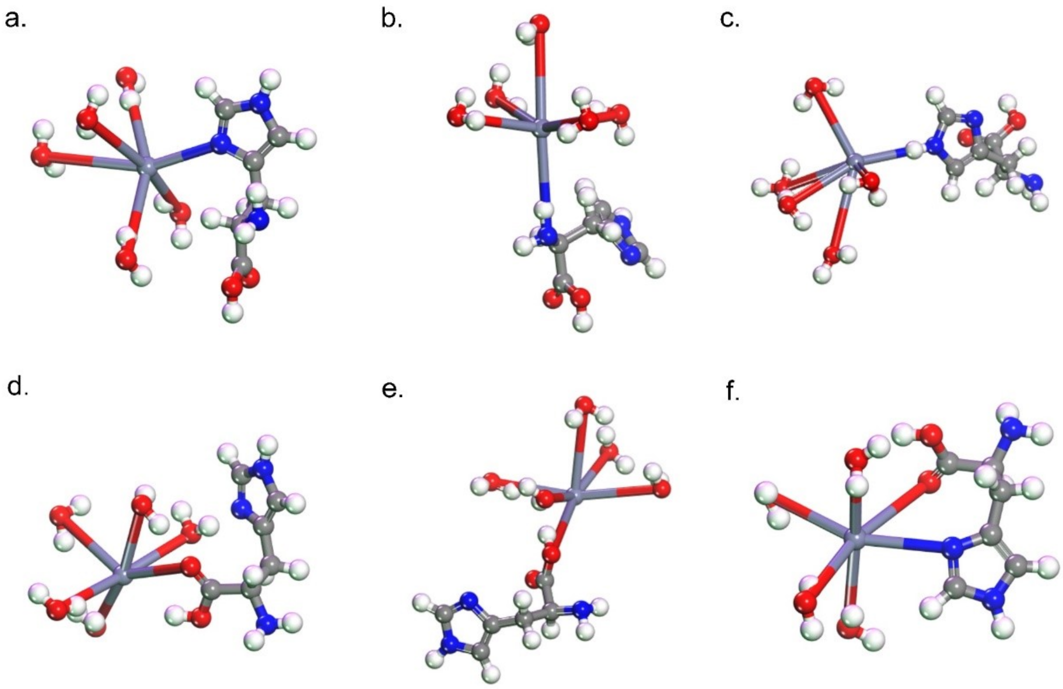

Figure S18 The different coordination configurations when histidine addition: (a) N1 site refers to the nitrogen atom in the guanidyl group with a double bond, (b) N2 site, indicating the nitrogen atom in the amino group, (c) N3 site, denoting the nitrogen atom in the guanidyl group with a single bond, (d) O1 site, representing the oxygen atom in the carbonyl group, (e) The O2 site involves the hydroxyl group coordinated with zinc ions, (f) O1, N1 site is the double-anchored site on the anode with the oxygen atom in the carbonyl group and the nitrogen atom in the guanidyl group with a double bond.

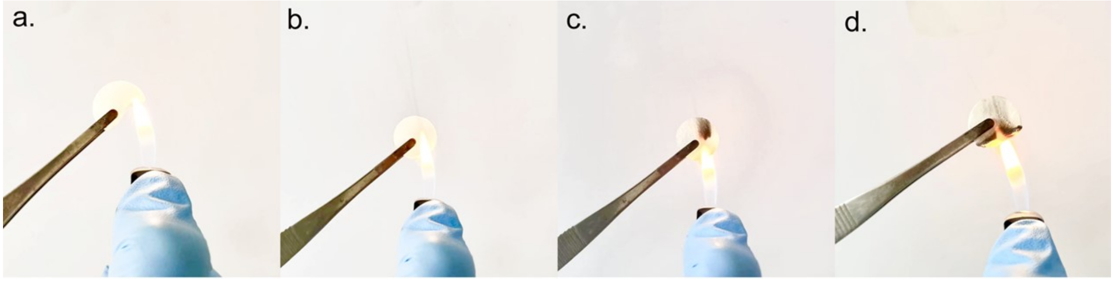

Figure S19 Flame retardant test of different electrolytes: (a) normal glass fiber separator, (b) glass fiber separator soaked into 0.1M arginine, (c) glass fibber separator soaked into 0.02M histidine, (d) glass fiber separator soaked into baseline electrolyte.

Figure S20 After the flame-retardant test of different electrolytes, the morphology of the glass fiber: (a) normal glass fiber separator, (b) glass fiber separator soaked into baseline electrolyte. (c) glass fiber separator soaked into 0.1M arginine, (d) glass fiber separator soaked into 0.02M histidine.

Based on the flame-retardant test results, the untreated normal glass fiber exhibited evident melting traces. Following immersion in the baseline solution, there was a slight improvement observed. However, when comparing the morphologies after immersion in solutions containing histidine and arginine, it was observed that the morphology obtained with 0.1M arginine exhibited the most favorable characteristics, surpassing even that obtained with 0.02M histidine. Despite histidine having a higher melting point compared to arginine, the lower concentration of histidine resulted in inferior flame-retardant properties.

Charge Density Difference Analysis

Charge Density Difference (CDD) is a widely used analytical technique to investigate charge redistribution by comparing the charge densities of the system of interest with those of a reference system[64,65]. In our study, we employ CDD to illustrate how the adsorption of amino acids induces unbalanced charge distribution on the zinc surface, thereby accelerating Zn^{2+} diffusion and deposition through electrostatic attraction towards Zn^{2+}. Notably, serine exhibits the largest contact isosurface with the zinc anode, indicating the strongest interaction with the anode surface, which confirms the evidence of the highest adsorption energy. The charge density results from a side view in Figure S21 and from a top view in Figure S22 show pink and blue regions representing electron accumulation and depletion, respectively. This suggests that electrons tend to transfer from the amino acid molecules to the Zn surface, indicating strong adsorption between the additive molecules and the Zn atoms.

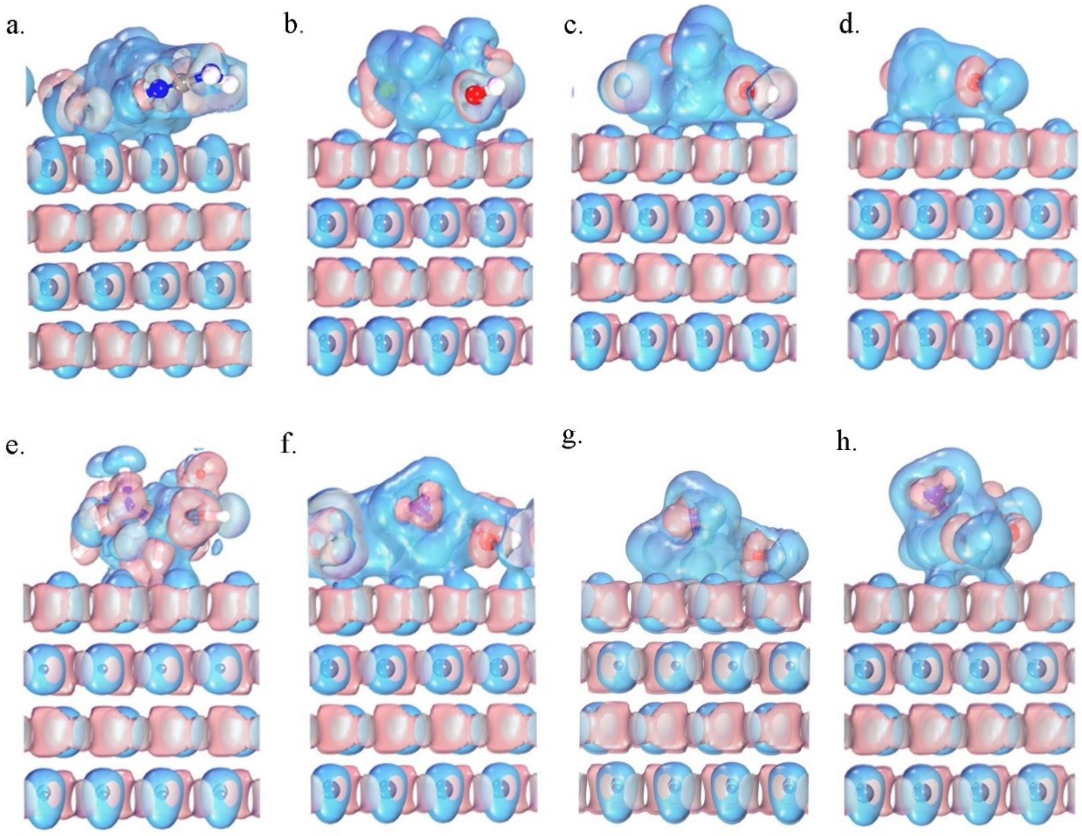

Figure S21 The charge energy difference of (a) arginine (b) cysteine (c) glutamic acid (d) glycine (e) histidine (f) lysine (g) serine (h) threonine.

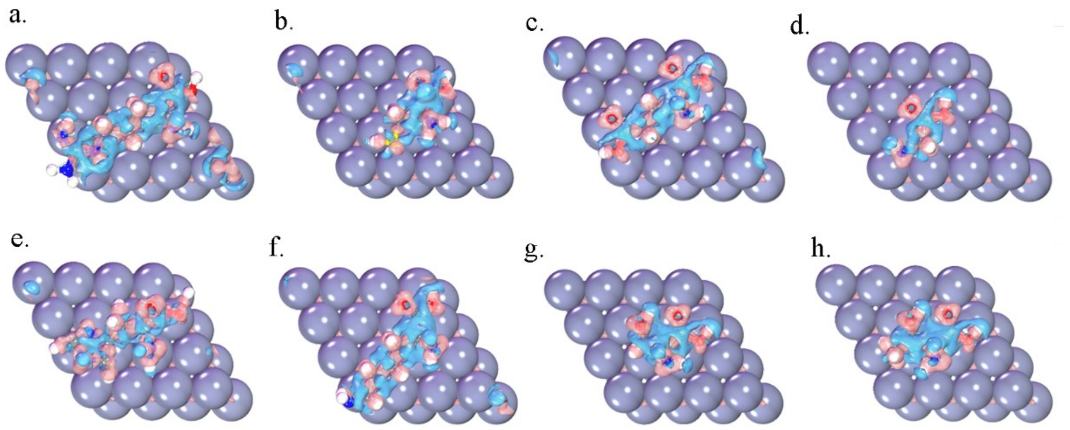

Figure S22 The electron density analysis based on the adsorption model in the side view with the addition of additives: (a) arginine (b) cysteine (c) glutamic acid (d) glycine (e) histidine (f) lysine (g) serine (h) threonine.

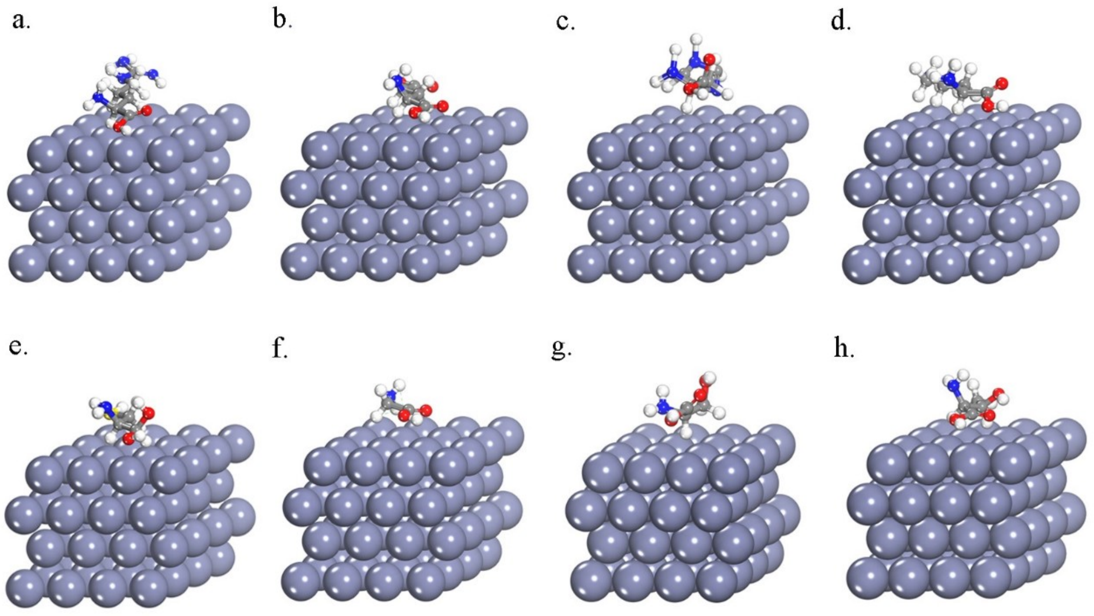

Figure S23 The adsorption model of polar charged amino acids (a) arginine, (b) glutamic acid, (c) histidine, and (d) lysine. The adsorption model of polar uncharged amino acids (e) cysteine, (f) glycine, (g) serine, and (h) threonine.

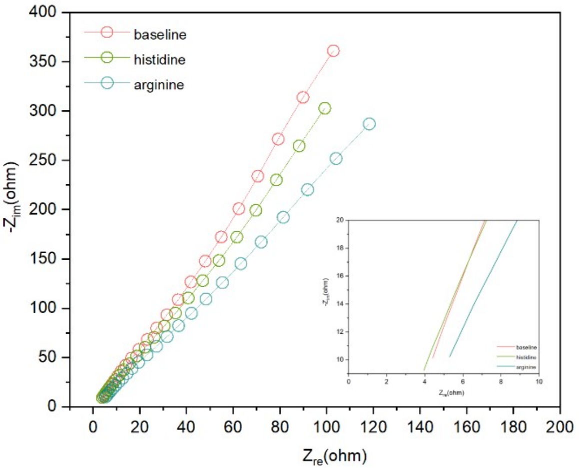

Figure S24 SS//SS EIS plots with different electrolytes, i.e., baseline, with the addition of histidine and with the addition of arginine.

Ionic conductivity is a crucial parameter for assessing electrolyte properties. To measure the ionic conductivity of various electrolyte systems, EIS was employed using a two-electrode configuration with SS//SS. The ionic conductivity (σ) of the solution was determined using formula (6):

$$\sigma = l / R_0 S \qquad (6)$$

σ represents the ionic conductivity (S cm^{-1}) and l denotes the thickness of the electrolyte. R_0 represents the ohmic impedance. S signifies the contact area between the electrolyte and electrodes.

Ionic conductivity is a critical property of electrolytes, reflecting their ability to conduct ions and their resistance to such conduction. In SS//SS cells, impedance measurements primarily reflect ohmic impedance due to the absence of electrochemical reactions, thereby eliminating the influence of electrochemical and concentration impedances. Hence, we utilized EIS to examine the ohmic impedance of SS///SS cells[38]. Ohmic impedance (R_Ω) is identified as the point where the high-frequency segment of the EIS spectrum intersects the horizontal axis, representing the intrinsic resistance of the electrolyte. Our analysis reveals that the ohmic impedance is higher in electrolytes containing arginine compared to the control group. This suggests a progressive rise in resistance to both anion and cation transport within the electrolyte. Conversely, with the inclusion of histidine, the ohmic impedance is lower than in the control group, indicating an ensuing enhancement in conductivity. With varying additive concentrations, the resulting ionic conductivities were as follows: 0.0304 S cm^{-1} for the electrolyte containing 1M ZSO, 0.0328 S cm^{-1} for the electrolyte with 0.02M histidine additive, and 0.0280 S cm^{-1} for the electrolyte with 0.1M arginine additive.

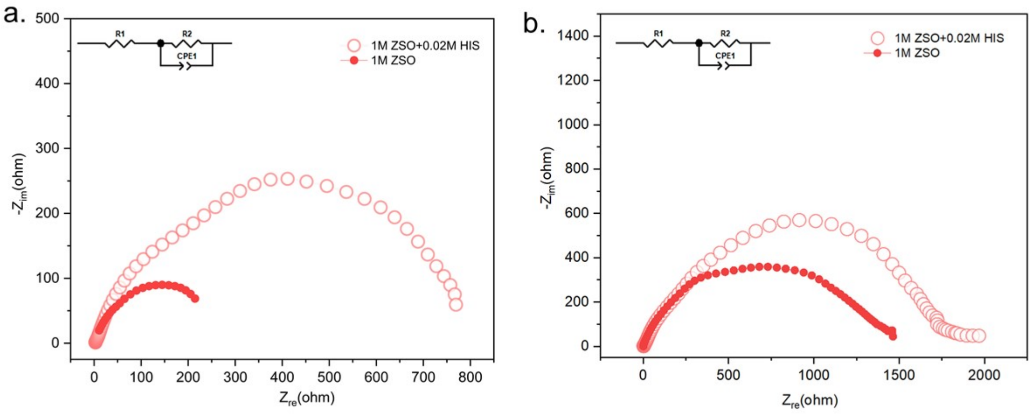

Figure S25 The EIS plots of the Zn//Zn battery with histidine addition when (a) no polarization and (b) polarized by 20mV.

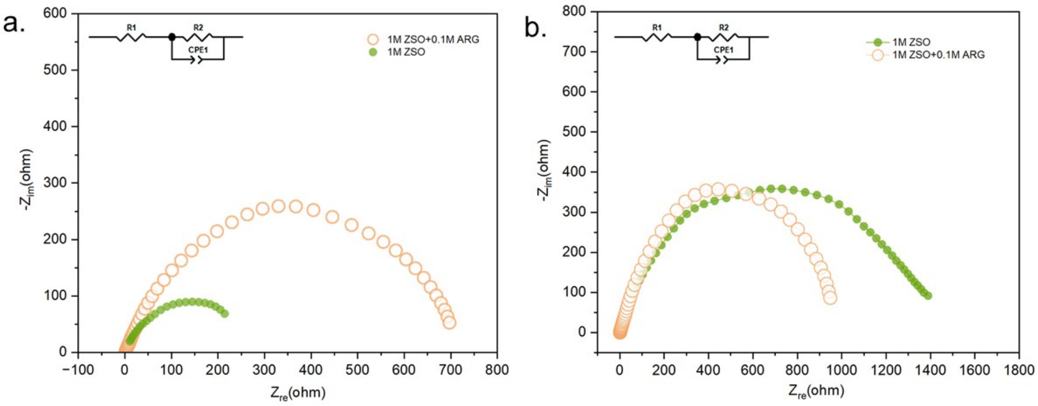

Figure S26 The EIS plots of the Zn//Zn battery with arginine addition when (a) no polarization and (b) polarized by 20mV.

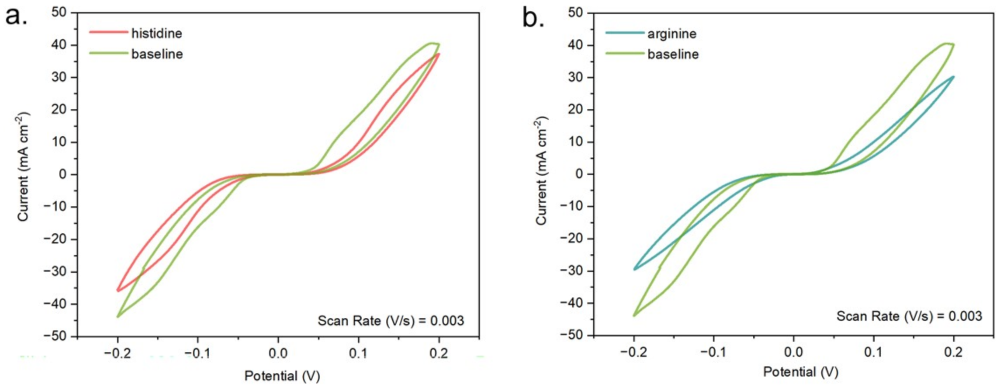

Figure S27. CV curves of Zn//Zn symmetric cells in a voltage range of −200 mV to 200 mV under various scanning rates in the ZSO electrolyte (a) with histidine (b) with arginine.

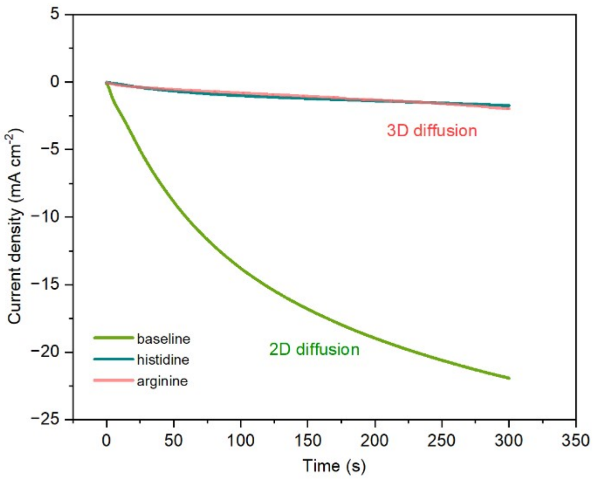

Figure S28. CA curves for Zn electrodes with different electrolytes.

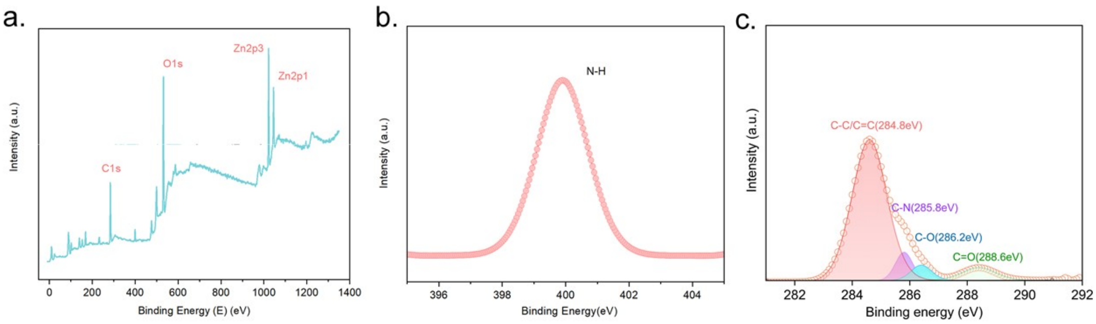

Figure S29 (a) XPS survey spectrum, (b) N1s XPS spectrum of zinc foil cycled with the addition of histidine. (c) O1s XPS spectrum of zinc foil cycled with the addition of histidine.

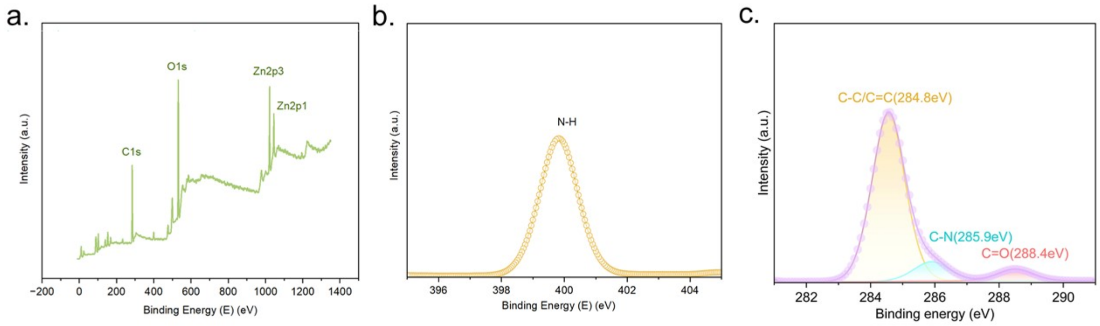

Figure S30 (a) XPS survey spectrum, (b) N1s XPS spectrum of zinc foil cycled with the addition of arginine. (c) O1s XPS spectrum of zinc foil cycled with the addition of arginine.

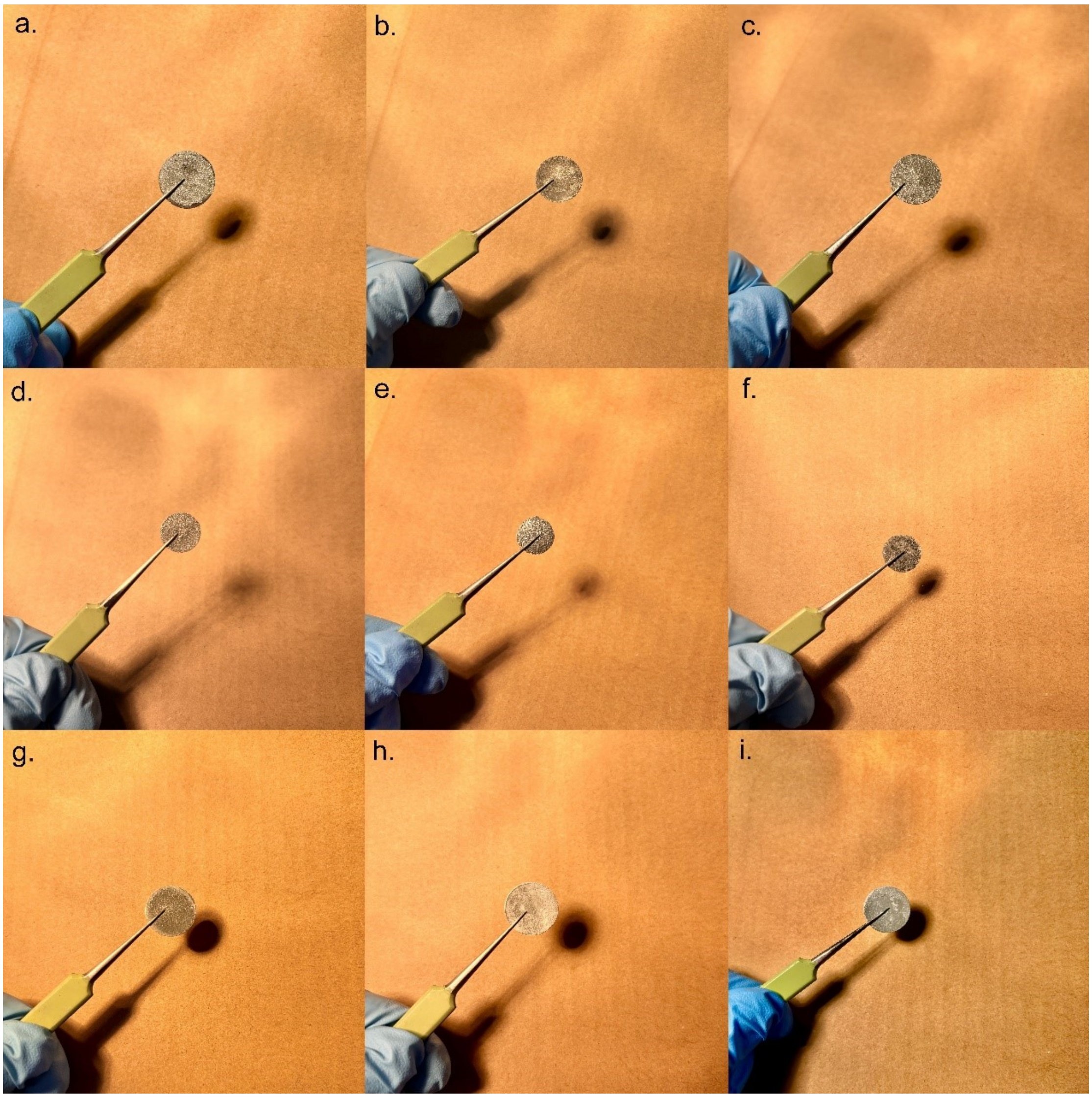

Figure S31 The deposition morphology of cycled zinc foil. Under the current density of 40 mA cm^{-2} and 40 mAh cm^{-2}, the Zn//Zn battery cycled (a) in 1M ZSO, (b) with 0.1M arginine addition, (c) with 0.02M histidine addition. Under the current density of 5 mA cm^{-2} and 1 mAh cm^{-2}, the Zn//Cu battery cycled (d) with 0.02M histidine addition, (e) with 0.1M arginine addition, (f) in 1M ZSO. Under the current density of 5 mA cm^{-2} and 10 mAh cm^{-2}, the Zn//Zn battery cycled (g) with 0.02M histidine addition, (h) with 0.1M arginine addition, (i) in 1M ZSO.

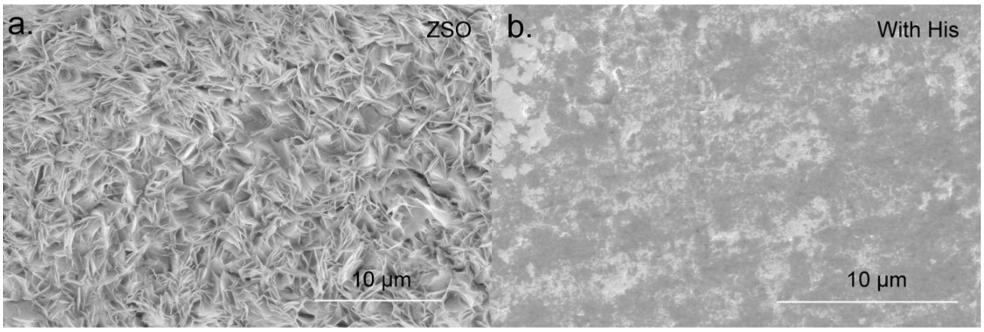

Figure S32 SEM images in the small scale with zinc foil soaked in the solution for 1200h (c) without histidine and (d) with histidine addition.

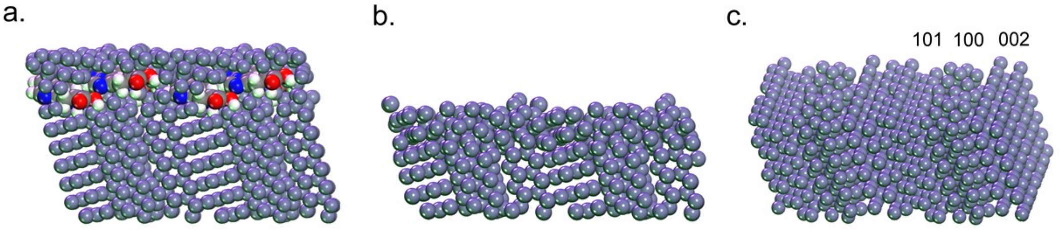

Figure S33 The deposition behavior of zinc ions with and without histidine addition simulated by DFT calculations.

The Choice for Zinc Deposition Facet

Recent investigations have highlighted the efficacy of texturing the Zn (002) crystal plane during Zn^{2+} deposition to suppress dendrites and mitigate side reactions. The Zn (002) crystal plane exhibits a high activation energy for dissolving zinc, significantly reducing the likelihood of undesirable effects during cycling. The roughness of the low-index Zn (002) crystal plane leads to a decreased corrosion current, inhibiting zinc dendrite formation. Furthermore, the constant interfacial charge density on the low-index Zn (002) crystal plane reduces the chances of zinc breaching the separator, promoting uniform Zn^{2+} deposition with a crystal orientation parallel to the initial Zn (002). The tightly packed atomic arrangement of the low-index Zn (002) crystal plane contributes to the higher activation energy for zinc dissolution and decreased electrochemical activity. In contrast, the typical Zn (101) and Zn (110) crystal planes, being primarily vertically oriented to the Zn surface, are more prone to dendritic formation. To achieve dendrite-free anodes with uniform Zn^{2+} deposition, the hexagonal structure of the Zn (002) crystal plane in parallel alignment to the Zn surface proves advantageous[66].

The relative texture coefficient (RTC) calculation:

For characterizing the crystallographic orientation of the Zn electrode, as one of the most important indicators, the RTC for three representative crystal planes was further calculated via the following formula[67].

$$RCT_{(hkl)} = \frac{I_{(hkl)}/I_{0(hkl)}}{\sum(I_{(hkl)}/I_{0(hkl)})} \times 100 \qquad (7)$$

where the characters $RTC_{(hkl)}$, $I_{(hkl)}$, and $I_{0(hkl)}$ represent, respectively, the texture coefficient of the (hkl) plane, the actual diffraction intensity of the (hkl) plane in the XRD for the employed Zn plate, and the diffraction intensity of the (hkl) plane for the standard Zn plate (PDF#04-0831).

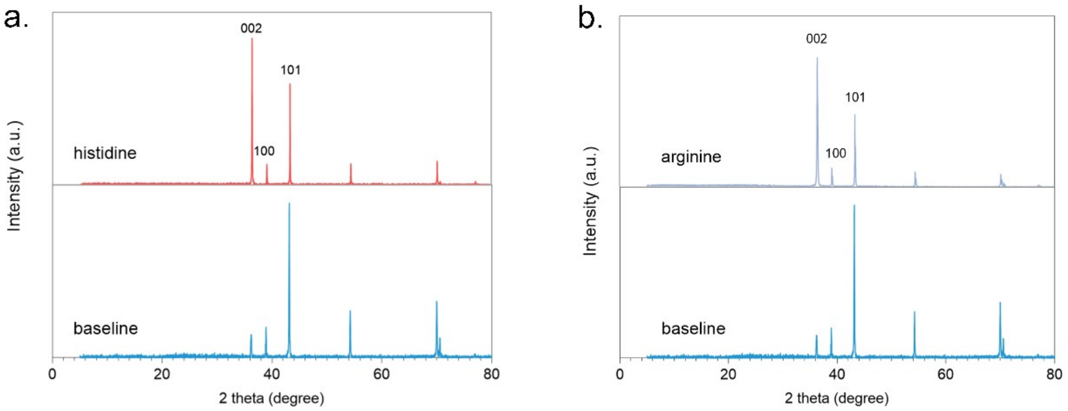

Figure S34 (a) The comparison of the XRD patterns of the cycled Zn foils with baseline and with histidine addition. (b) The XRD comparisons of the cycled Zn foil with baseline and arginine addition.

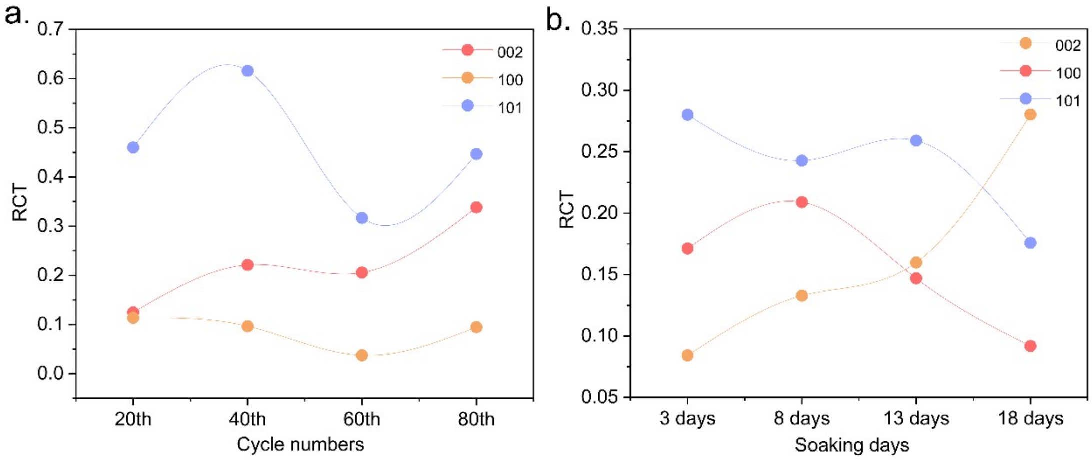

Figure S35 (a) The corresponding fitted RTCs of Zn (002), Zn (100), and Zn (101) planes after analyzing the XRD patterns of the surface of the Zn plate after different cycles in electrolytes with histidine. (b) The corresponding line chart for the fitted RTCs of Zn (002), Zn (100), and Zn (101) planes after analyzing the XRD patterns of the surface of Zn plate soak in the electrolyte with histidine addition.

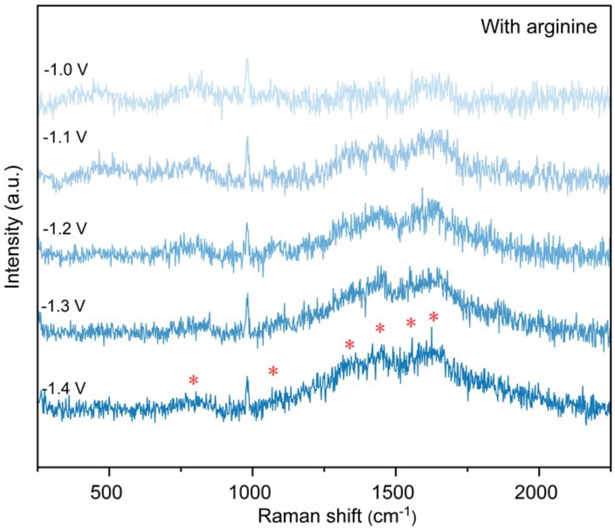

Figure S36 The in-situ Raman analysis of the anode-electrolyte surface at different voltages with the addition of arginine.

Table S3 The corresponding peak value of histidine in the Raman spectrum.

Raman (cm^{-1})[68] (histidine in aqueous solution)	Assignment (PED)[68]
1573	Cγ-Cδ (23), Cβ-Cγ (13), Nδ-Cγ-Cδ (11)
1500	Nε-Cε (24), Nδ-Cε-H (12), Nε-Cε-H (11), Nε-Cε-H (11)
1443	CtOO$^-$ sym. st. (25), Cα-Ct (14), Cβ-rock. (11)
1409	Nt-Cα-Hα (33), Cβ-Cα-H (23), Cβ-rock. (22)
1355	Nδ-Cε (20), Cβ-twist. (16), Cγ-Nδ (12)
1319	NtH_3^+ asym. rock. (24), Cβ-rock. (15), Ct-Cα-H (10)
1272	Nδ-Cε-H (28), Cγ-Cδ-H (11)
1113	NtH_3^+ asym. rock. (38), Ctγ-Cαγ-H (20)
1088	Cγ-Nε (26),Nε-Cδ-H (11), Nε-Cε (11)
854	ω (Cε-H) (81)
784	ω (Cε-H) (73)

Table S4 The corresponding peak value of arginine in the Raman spectrum.

Raman (cm^{-1})[69] (arginine in aqueous solution)	Assignment (PED)[69]
860	τ (Cζ-Nη2) (25); W7
1092	CζN η H_2 asym bend (62)
1353	CtOO$^-$ sym st (25); Nt-Cα-Hα (25); Cβ-Cα-Hα (17)
1445	Nη1-Cζ-Nη2 asym st (24); Cδ-Nε-Hε (22); Cζ-Nε-Hε (13); W6
1594	Nε-Cζ (17); H-O-H (W8) (13)
1605	Nη1-H_2 bend (42); Nη1-Cζ-Nη2 asym st (19); CζN η $2H_2$ sym bend (17)

asym, asymmetric; st, stretch; sym, symmetric; ω, out-of-plane bending; PED, potential energy distribution; Ct and Nt refer to the carbon and nitrogen atoms of the terminal COO^- and NH_3^+ groups, respectively.

Nucleation Overpotential (NOP) Calculation

The electro-deposition of Zn^{2+} typically involves several key processes: mass transfer, de-solvation, charge transfer, and electro-crystallization (nucleation and growth)[70,71]. The driving force for these processes, denoted as η, is defined as the difference between the actual electrode potential and the equilibrium electrode potential (Eq, 0 V for a Zn//Zn cell). According to the Butler-Volmer equation, η is influenced by both the polarization current density (j, an external cause) and the exchange current density (j_0, an internal cause dependent on factors such as electrode characteristics, salt type, and electrolyte concentration). Voltage–time profiles during Zn^{2+} electro-deposition offer insights into the significance of η. Upon the application of voltage, the potential rapidly shifts, leading to the formation of crystal nuclei on the Zn metal surface (initial substrate) once it reaches its peak value. This stage corresponds to the nucleation process, which may occur instantaneously or progressively, and can be denoted as η_n. Subsequently, η decreases as crystal growth requires less driving force compared to nucleus formation. Upon reaching a plateau in the curve, the voltage difference is termed η_g. Both η_n and η_g encompass contributions from the mass transfer, de-solvation, charge transfer, and electro-crystallization processes. During the transition from the point of one end of the platform to the other, controlled by both nucleation and growth processes, the required driving force is expressed as $\Delta\eta$. This process involves the interplay of various factors influencing η, highlighting the dynamic nature of Zn^{2+} electro-deposition. According to this equation, as the nucleation overpotential (NOP) increases, the critical nucleus radius decreases. Therefore, the introduction of an additive decreases the NOP value and increases the cathodic process area, indicating the promotion of electrocrystallization.

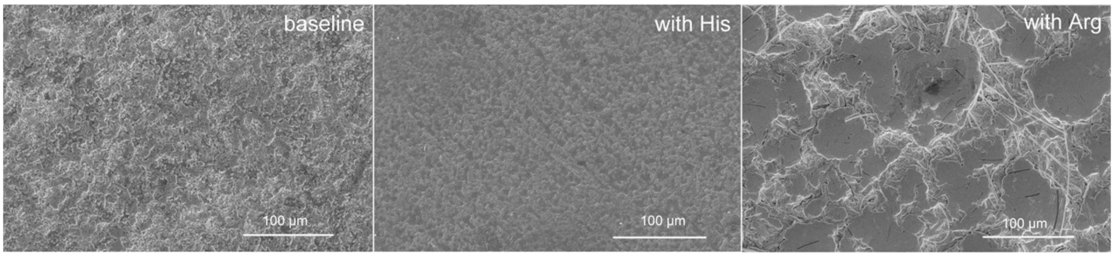

Figure S37 The SEM images after zinc foil cycled from Zn//Cu with or without additives.

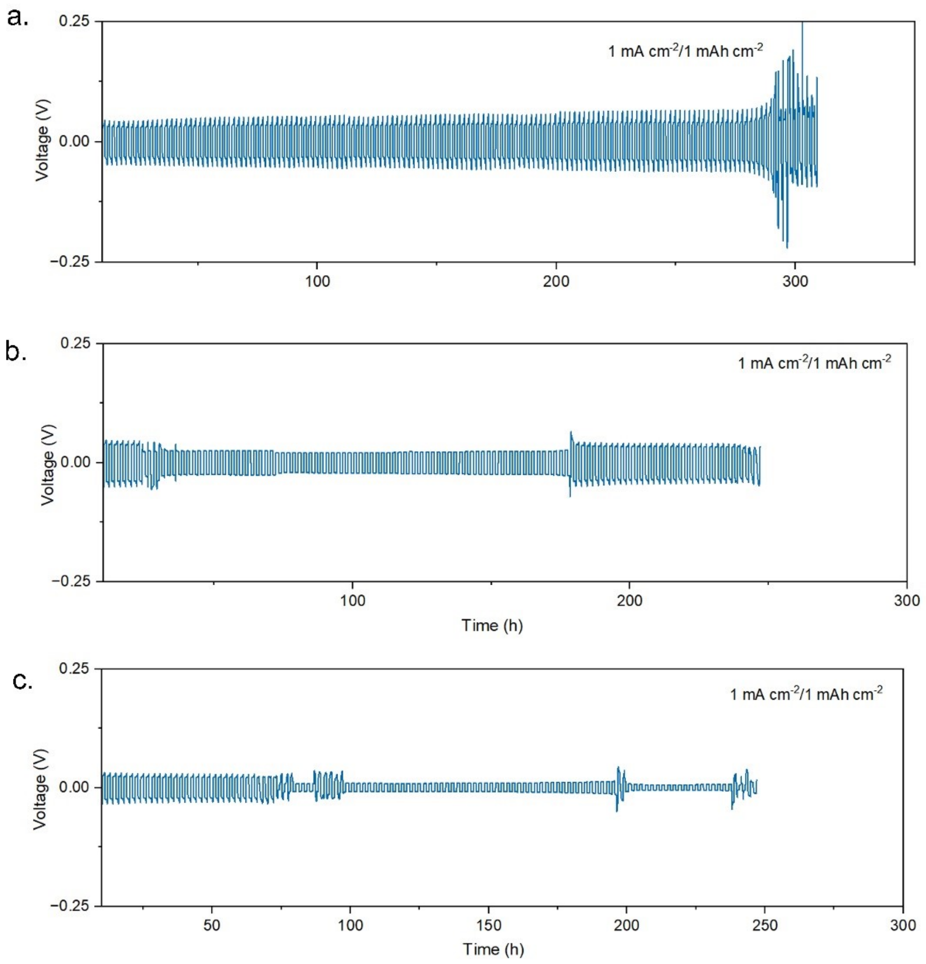

Figure S38 Cycling performance of the different concentrations of ZSO at the current density of 1mA cm^{-2} and 1mAh cm^{-2}: (a) 1M ZSO, (b) 5M ZSO, (c) 3M ZSO.

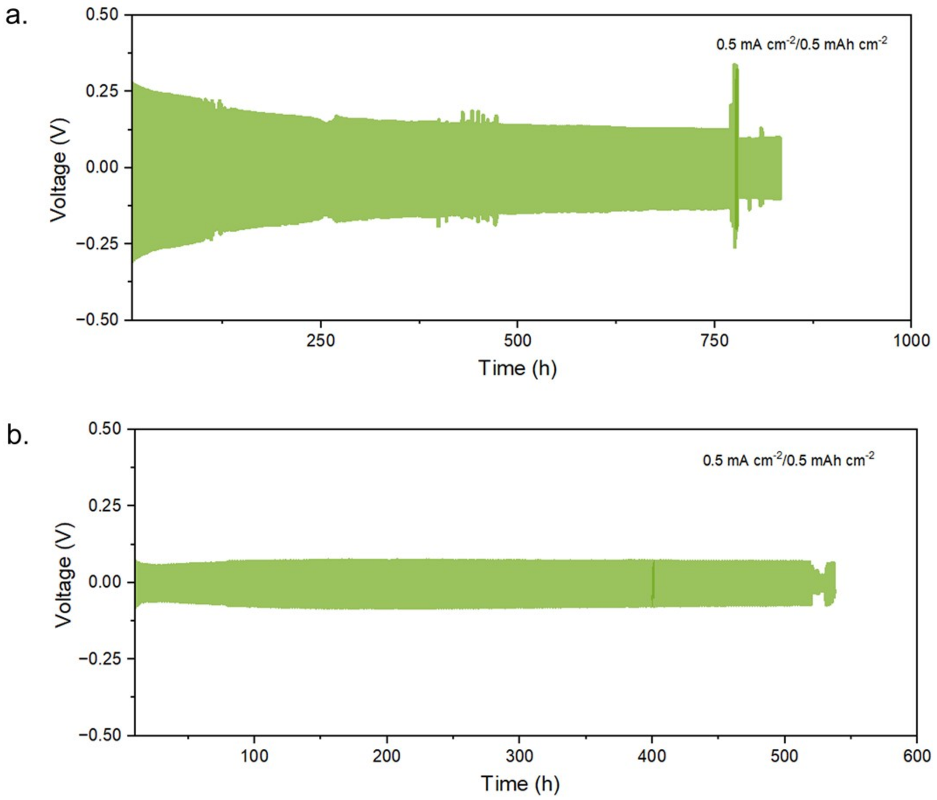

Figure S39 Cycling performance of Zn//Zn with the addition of different types of amino acids in the condition of the same concentration: (a) 0.1M glutamic acid, (b) 0.1M serine.

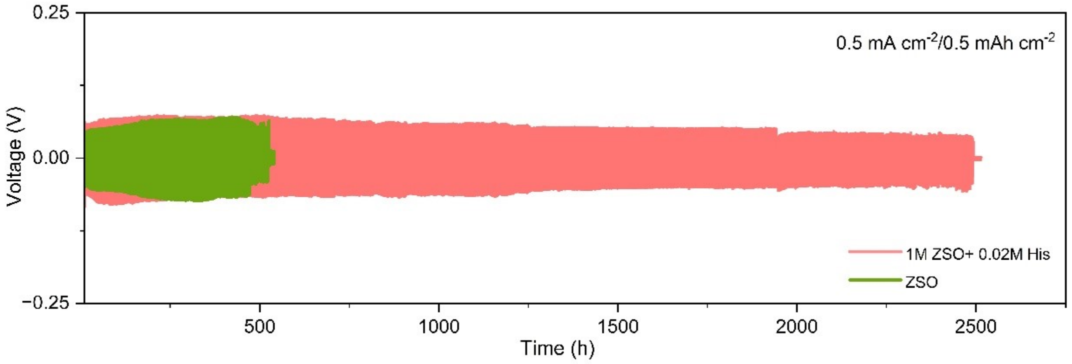

Figure S40 The cycling life of Zn//Zn with histidine acts as the additive at the current density of 0.5 mA cm^{-2} and 0.5 mAh cm^{-2}.

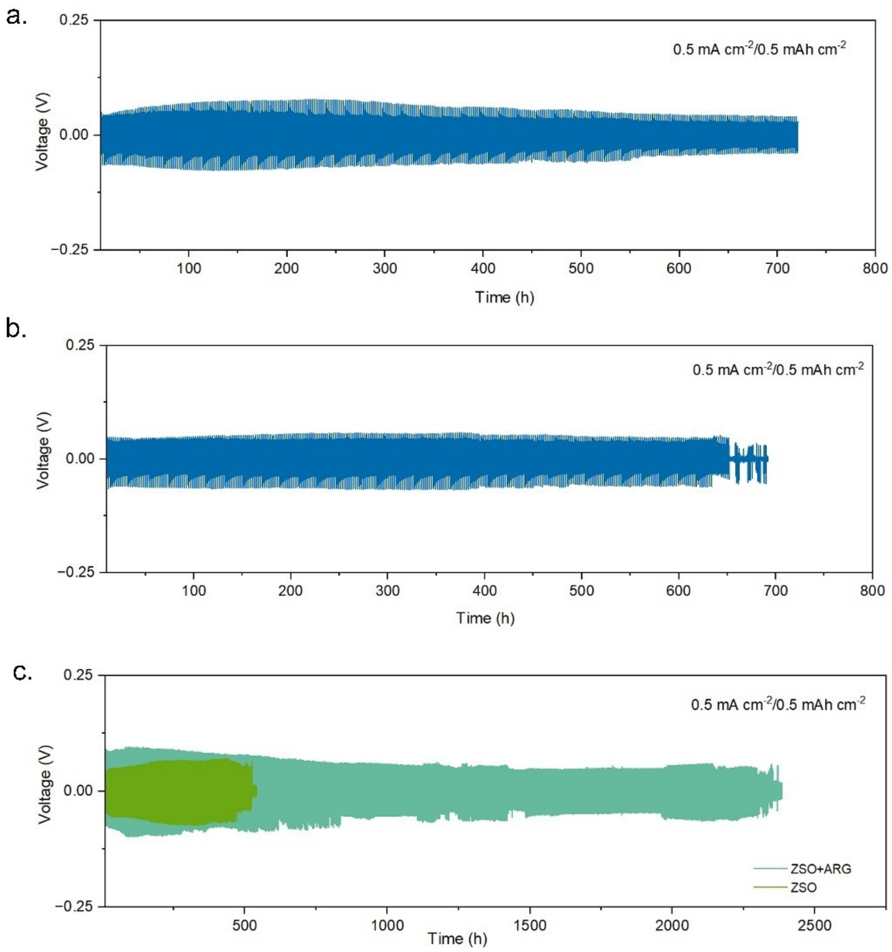

Figure S41 Cycling performance comparison of different concentrations of arginine, at the current density of 0.5 mA cm^{-2} & 0.5 mAh cm^{-2} when choosing 1M ZSO as the baseline: (a) 0.05M arginine, (b) 0.2M arginine, (c) 0.1M arginine.

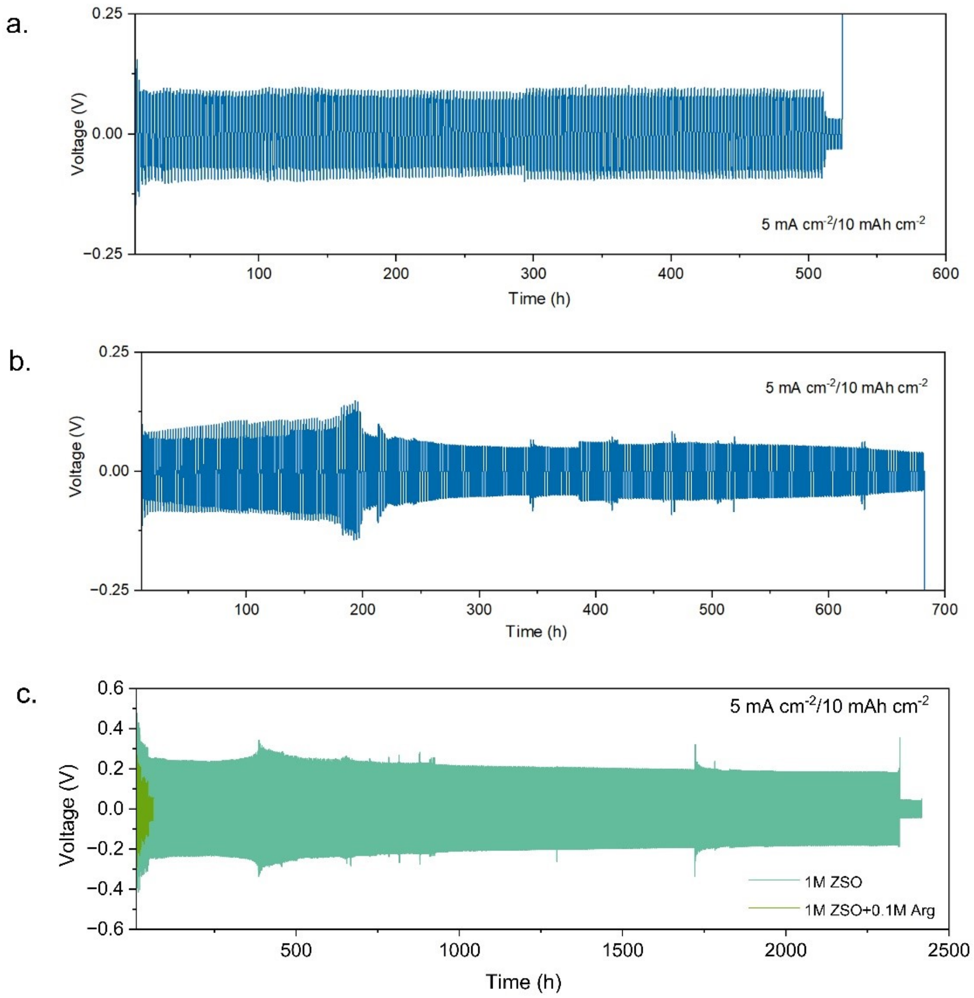

Figure S42 Cycling performance of Zn//Zn with the addition of different concentrations of arginine: (a) 0.2M, (b) 0.05M, (c) 0.1M (still lasting), at the current density of 5 mA cm^{-2} & 10 mAh cm^{-2}.

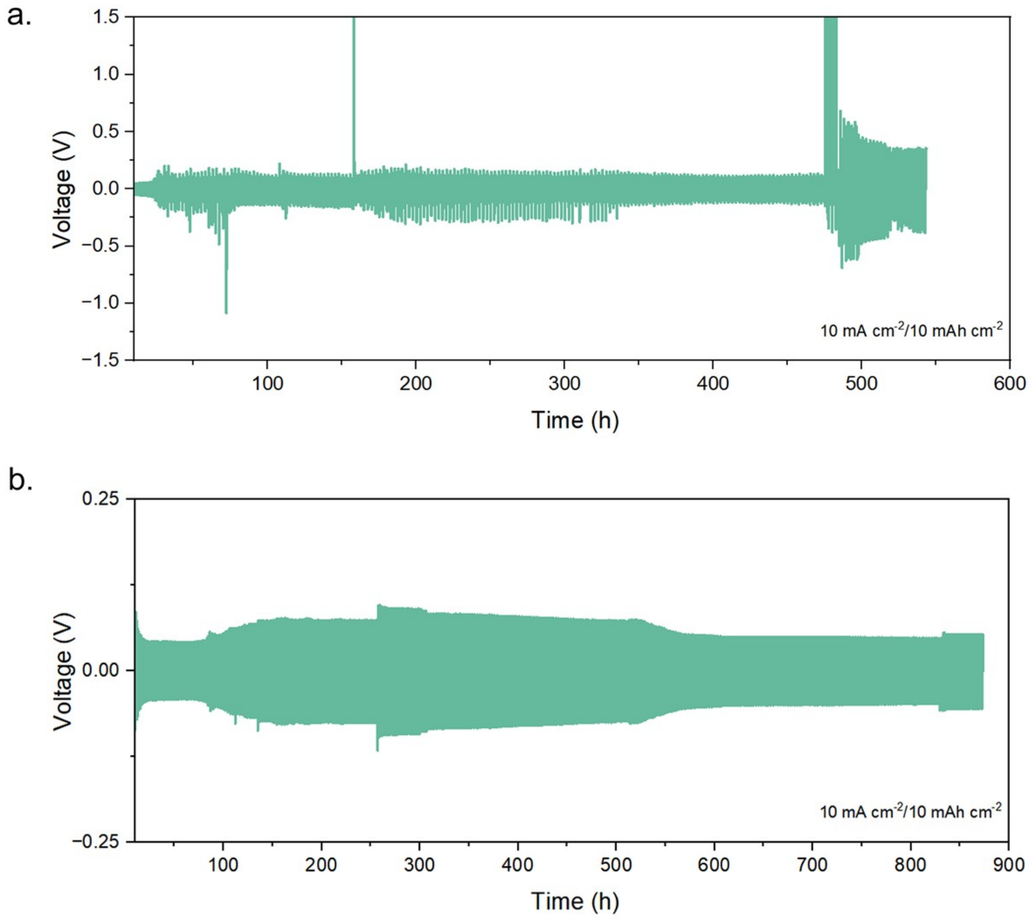

Figure S43 Cycling performance comparison of different concentrations of arginine, at the current density of 10 mA cm^{-2} & 10 mAh cm^{-2} when choosing 1M ZSO as the baseline: (a) 0.2M arginine, (b) 0.05M arginine.

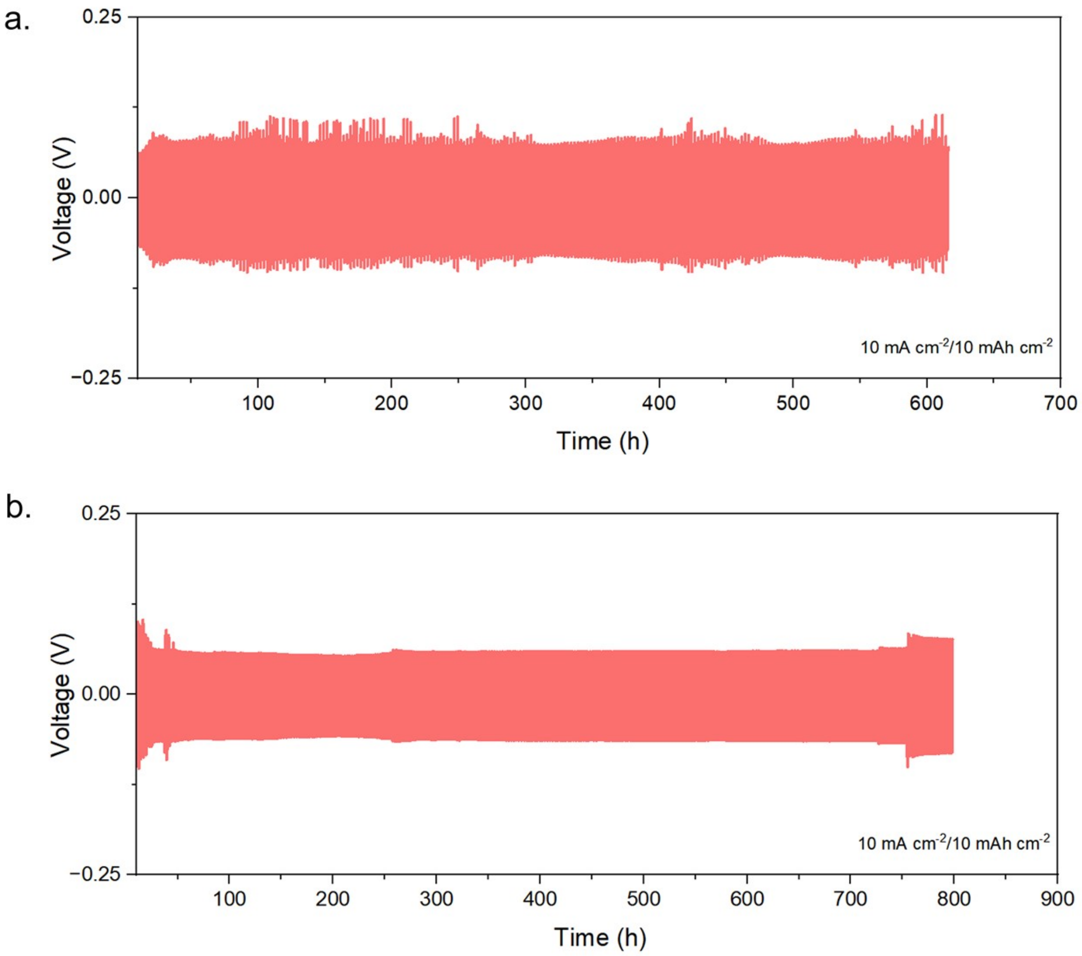

Figure S44 Cycling performance of Zn//Zn with the addition of different concentrations of histidine: (a) 0.1M, (b) 0.2M, at the current density of 10 mA cm^{-2} & 10 mAh cm^{-2}.

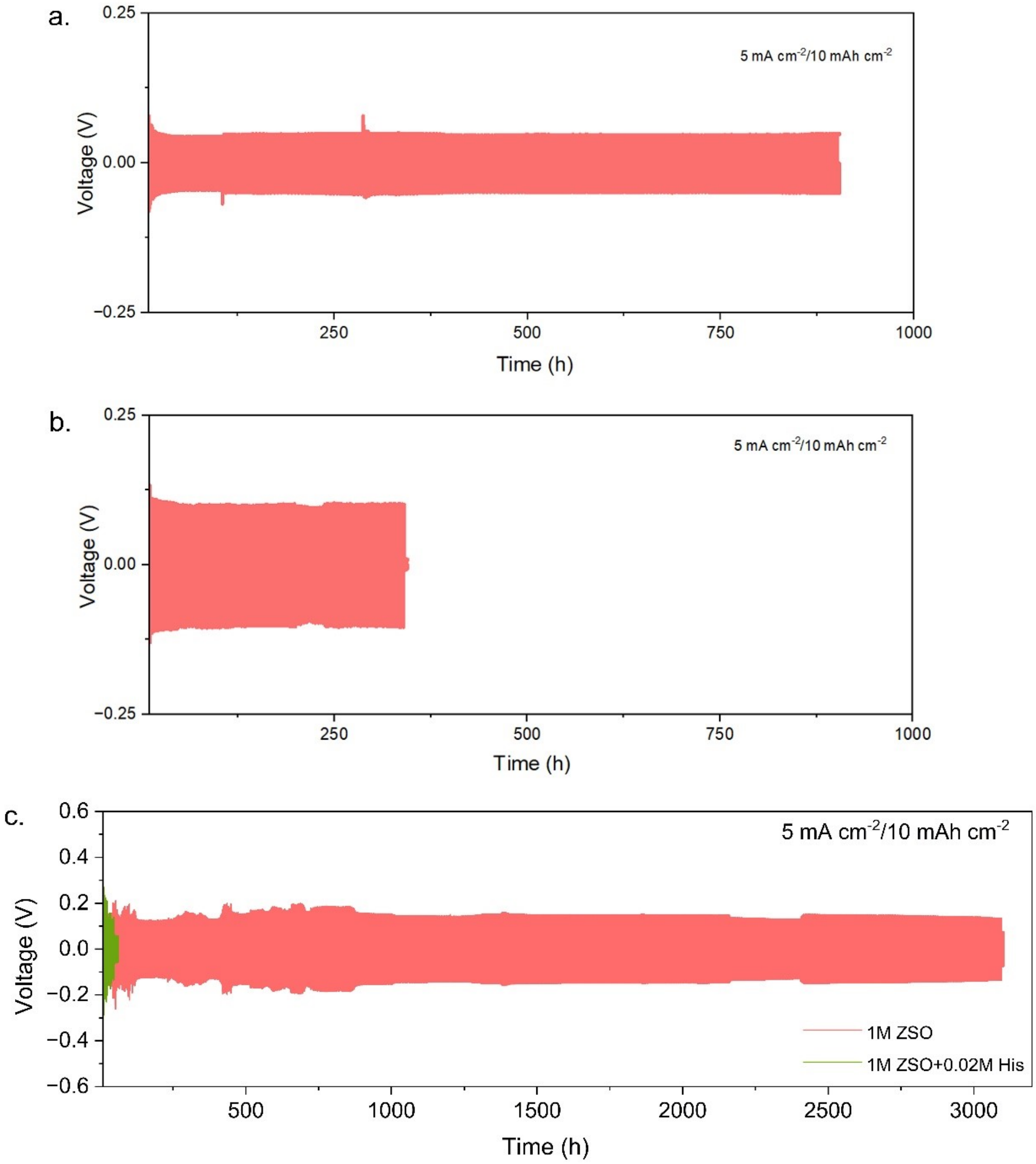

Figure S45 Cycling performance of Zn//Zn with the addition of different concentrations of histidine: (a) 0.1M, (b) 0.2M, (c) 0.02M, at the current density of 5 mA cm^{-2} & 10 mAh cm^{-2}.

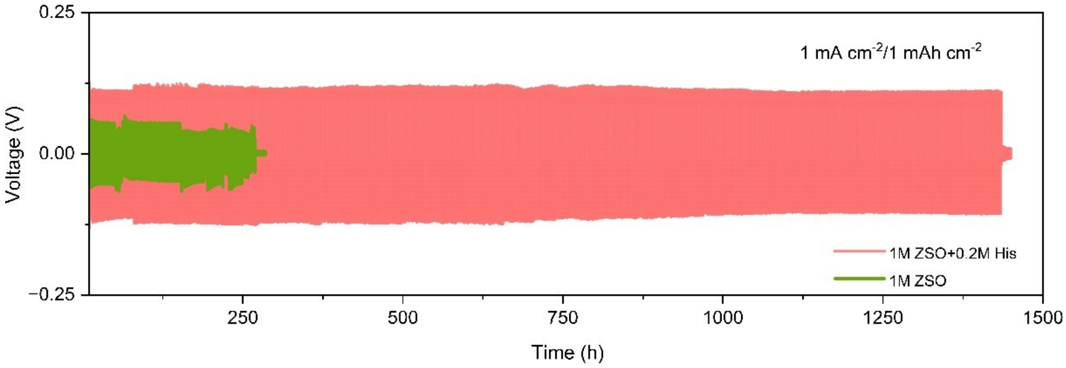

Figure S46 The cycling life of Zn//Zn with histidine acts as the additive at the current density of 1 mA cm^{-2} and 1 mAh cm^{-2}.

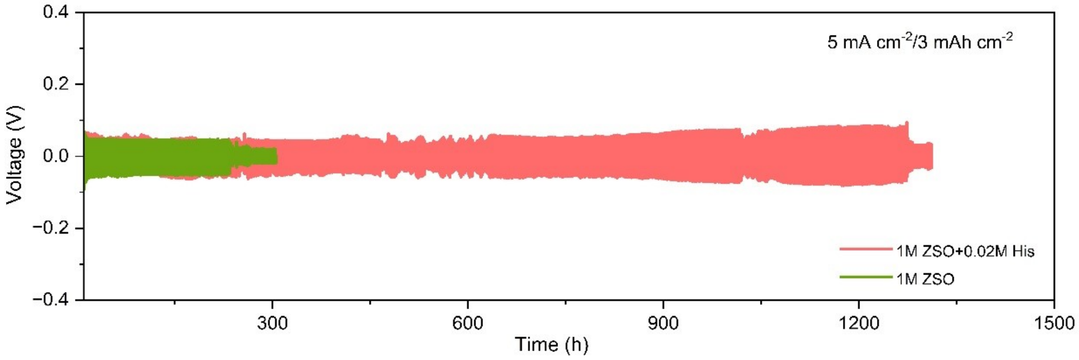

Figure S47 The cycling life of Zn//Zn with histidine acts as the additive at the current density of 5 mA cm^{-2} and 3 mAh cm^{-2}.

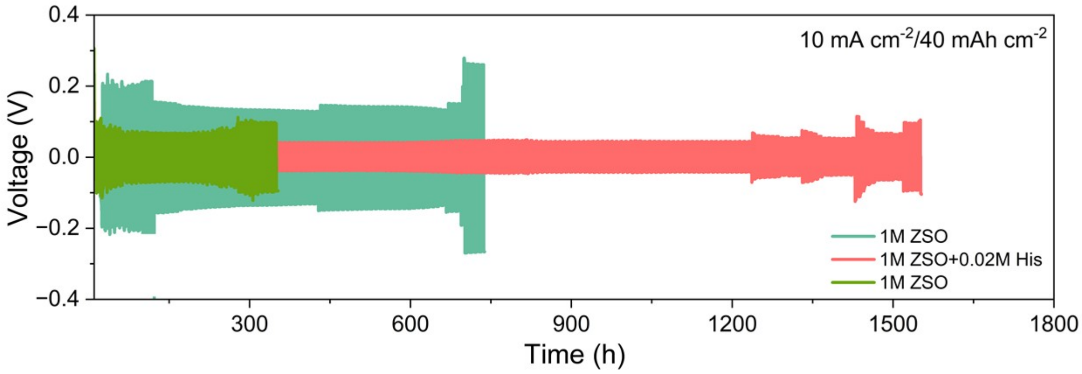

Figure S48 Comparison of voltage-time profiles for Zn stripping/plating of Zn//Zn symmetric cells during long-term cycling test at the current density: 10 mA cm^{-2} & 40 mAh cm^{-2}.

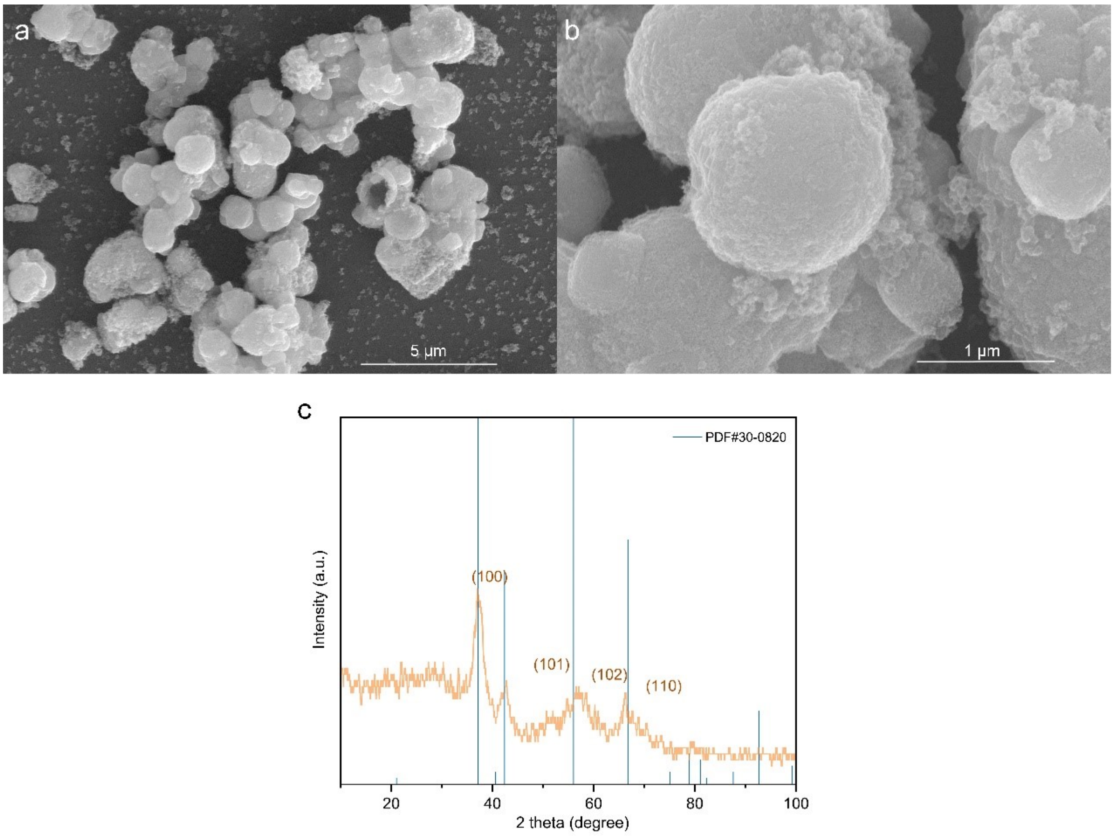

Figure S49 a, b The SEM images of MnO_2 morphology, c. XRD pattern of MnO_2.

REFERENCE

[1] N. Agmon, *Chemical Physics Letters* **1995**, *244*, 456–462.

[2] J. Zhu, L. Hu, P. Zhao, L. Y. S. Lee, K.-Y. Wong, *Chem. Rev.* **2020**, *120*, 851–918.

[3] X. Wang, G. Long, B. Liu, Z. Li, W. Gao, P. Zhang, H. Zhang, X. Zhou, R. Duan, W. Hu, C. Li, *Angew Chem Int Ed* **2023**, *62*, e202301562.

[4] F. Liu, C. Shi, X. Guo, Z. He, L. Pan, Z. Huang, X. Zhang, J. Zou, *Advanced Science* **2022**, *9*, 2200307.

[5] L. Zhang, X. Guo, S. Zhang, T. Frauenheim, S. Huang, *Advanced Energy Materials* **2024**, *14*, 2302754.

[6] Y. Lei, Y. Wang, Y. Liu, C. Song, Q. Li, D. Wang, Y. Li, *Angew Chem Int Ed* **2020**, *59*, 20794–20812.

[7] A. Raza, K. M. Deen, E. Asselin, W. Haider, *Renewable and Sustainable Energy*

Reviews **2022**, *161*, 112323.

[8] X. Liu, Y. Guo, F. Ning, Y. Liu, S. Shi, Q. Li, J. Zhang, S. Lu, J. Yi, *Nano-Micro Lett.* **2024**, *16*, 111.

[9] H. Cao, Q. Wang, Z. Zhang, H.-M. Yan, H. Zhao, H. B. Yang, B. Liu, J. Li, Y.-G. Wang, *J. Am. Chem. Soc.* **2023**, *145*, 13038–13047.

[10] G. Shao, C. Jing, Z. Ma, Y. Li, W. Dang, D. Guo, M. Wu, S. Liu, X. Zhang, K. He, Y. Yuan, J. Luo, S. Dai, J. Xu, Z. Zhou, *Nat Commun* **2024**, *15*, 385.

[11] H. Li, S. Xu, M. Wang, Z. Chen, F. Ji, K. Cheng, Z. Gao, Z. Ding, W. Yang, *J. Mater. Chem. A* **2020**, *8*, 17987–17997.

[12] W. Kong, J. Xu, Y. Tong, Y. Ding, J. Wang, B. Li, X. Wei, L. Zhao, *Phys. Chem. Chem. Phys.* **2022**, *24*, 29141–29150.

[13] R. Chen, W. Zhang, C. Guan, Y. Zhou, I. Gilmore, H. Tang, Z. Zhang, H. Dong, Y. Dai, Z. Du, X. Gao, W. Zong, Y. Xu, P. Jiang, J. Liu, F. Zhao, J. Li, X. Wang, G. He, *Angew Chem Int Ed* **2024**, e202401987.

[14] Z. Qu, J. Ma, Y. Huang, T. Li, H. Tang, X. Wang, S. Liu, K. Zhang, J. Lu, D. D. Karnaushenko, D. Karnaushenko, M. Zhu, O. G. Schmidt, *Advanced Materials* **2024**, 2310667.

[15] H. Tang, N. Hu, L. Ma, H. Weng, D. Huang, J. Zhu, H. Yang, Z. Chen, X. Yin, J. Xu, H. He, *Adv Funct Materials* **2024**, 2402484.

[16] Y. Chen, Z. Deng, Y. Sun, Y. Li, H. Zhang, G. Li, H. Zeng, X. Wang, *Nano-Micro Lett.* **2024**, *16*, 96.

[17] Z. Yang, C. Hu, Q. Zhang, T. Wu, C. Xie, H. Wang, Y. Tang, X. Ji, H. Wang, *Angew Chem Int Ed* **2023**, *62*, e202308017.

[18] M. Han, J. Zhang, C. Yu, J. Yu, Y. Wang, Z. Jiang, M. Yao, G. Xie, Z. Yu, J. Qu, *Angew Chem Int Ed* **2024**, e202403695.

[19] Y. Xia, R. Tong, J. Zhang, M. Xu, G. Shao, H. Wang, Y. Dong, C.-A. Wang, *Nano-Micro Lett.* **2024**, *16*, 82.

[20] Y. Li, P. Wu, W. Zhong, C. Xie, Y. Xie, Q. Zhang, D. Sun, Y. Tang, H. Wang, *Energy Environ. Sci.* **2021**, *14*, 5563–5571.

[21] H. Jiang, L. Tang, Y. Fu, S. Wang, S. K. Sandstrom, A. M. Scida, G. Li, D. Hoang, J. J. Hong, N.-C. Chiu, K. C. Stylianou, W. F. Stickle, D. Wang, J. Li, P. A. Greaney, C. Fang, X. Ji, *Nat Sustain* **2023**, *6*, 806–815.

[22] F. Zhang, T. Liao, H. Peng, S. Xi, D.-C. Qi, A. Micallef, C. Yan, L. Jiang, Z. Sun, *J. Am. Chem. Soc.* **2024**, jacs.4c01188.

[23] X. Chen, P. Gao, W. Li, N. A. Thieu, Z. M. Grady, N. G. Akhmedov, K. A. Sierros, M. Velayutham, V. V. Khramtsov, D. M. Reed, X. Li, X. Liu, *ACS Energy*

Lett. **2024**, 1654–1665.

[24] Y. Kang, F. Zhang, H. Li, W. Wei, H. Dong, H. Chen, Y. Sang, H. Liu, S. Wang, *Energy & Environ Materials* **2024**, e12707.

[25] M. Zhang, W. Xu, X. Han, H. Fan, T. Chen, Y. Yang, Y. Gao, C. Zheng, Y. Yang, T. Xiong, Y. Zhang, W. S. V. Lee, W. Wang, H. Pan, Z. G. Yu, J. Xue, *Advanced Energy Materials* **2024**, *14*, 2303737.

[26] C. Huang, J. Mao, S. Li, W. Zhang, X. Wang, Z. Shen, S. Zhang, J. Guo, Y. Xu, Y. Lu, J. Lu, *Adv Funct Materials* **2024**, 2315855.

[27] H. Fan, H. Zhang, Q. Liu, M. Li, L. Liu, J. Gao, Q. Zhang, E. Wang, *ACS Energy Lett.* **2023**, *8*, 4338–4348.

[28] D. Lin, D. Shi, A. Zhu, C. Yang, T. Zhang, K. Liu, K. Liu, G. Hong, W. Zhang, *Advanced Energy Materials* **2024**, 2304535.

[29] H.-B. Chen, H. Meng, T.-R. Zhang, Q. Ran, J. Liu, H. Shi, G.-F. Han, T.-H. Wang, Z. Wen, X.-Y. Lang, Q. Jiang, *Angew Chem Int Ed* **2024**, e202402327.

[30] M. Wu, X. Wang, F. Zhang, Q. Xiang, Y. Li, J. Guo, *Energy Environ. Sci.* **2024**, *17*, 619–629.

[31] H. Du, Y. Dong, Q. Li, R. Zhao, X. Qi, W. Kan, L. Suo, L. Qie, J. Li, Y. Huang, *Advanced Materials* **2023**, *35*, 2210055.

[32] Z. Zhang, P. Wang, C. Wei, J. Feng, S. Xiong, B. Xi, *Angew Chem Int Ed* **2024**, e202402069.

[33] D. Wang, H. Peng, S. Zhang, H. Liu, N. Wang, J. Yang, *Angewandte Chemie* **2023**, e202315834.

[34] N. Hu, W. Lv, W. Chen, H. Tang, X. Zhang, H. Qin, D. Huang, J. Zhu, Z. Chen, J. Xu, H. He, *Adv Funct Materials* **2024**, *34*, 2311773.

[35] S. Yang, A. Chen, Z. Tang, Z. Wu, P. Li, Y. Wang, X. Wang, X. Jin, S. Bai, C. Zhi, *Energy Environ. Sci.* **2024**, *17*, 1095–1106.

[36] X. Shi, J. Xie, J. Wang, S. Xie, Z. Yang, X. Lu, *Nat Commun* **2024**, *15*, 302.

[37] H. Li, L. Yang, S. Zhou, J. Li, Y. Chen, X. Meng, D. Xu, C. Han, H. Duan, A. Pan, *Adv Funct Materials* **2024**, 2313859.

[38] Q. Wu, J. Huang, J. Zhang, S. Yang, Y. Li, F. Luo, Y. You, Y. Li, H. Xie, Y. Chen, *Angew Chem Int Ed* **2024**, e202319051.

[39] K. Qiu, G. Ma, Y. Wang, M. Liu, M. Zhang, X. Li, X. Qu, W. Yuan, X. Nie, N. Zhang, *Adv Funct Materials* **2024**, 2313358.

[40] J. Weng, W. Zhu, K. Yu, J. Luo, M. Chen, L. Li, Y. Zhuang, K. Xia, Z. Lu, Y. Hu, C. Yang, M. Wu, Z. Zou, *Adv Funct Materials* **2024**, 2314347.

[41] L. Wang, C. Shen, C. Huang, J. Chen, J. Zheng, *ACS Nano* **2023**, *17*, 24619–24631.

[42] Z. Wang, Z. Hu, M. Ye, J. Chen, Y. Chen, Z. Wen, Y. Zhang, Y. Tang, X. Liu, C. C. Li, *Chemical Engineering Journal* **2024**, *481*, 148511.

[43] T. Yan, M. Tao, J. Liang, G. Zheng, B. Wu, L. Du, Z. Cui, H. Song, *Energy Storage Materials* **2024**, *65*, 103190.

[44] K. Yang, H. Fu, Y. Duan, Z. Ma, D. Wang, B. Li, H. S. Park, D. Ho, *ACS Energy Lett.* **2024**, *9*, 209–217.

[45] C. Huang, X. Zhao, Y. Hao, Y. Yang, Y. Qian, G. Chang, Y. Zhang, Q. Tang, A. Hu, X. Chen, *Energy Storage Materials* **2024**, *65*, 103158.

[46] X. Wang, K. Feng, B. Sang, G. Li, Z. Zhang, G. Zhou, B. Xi, X. An, S. Xiong, *Advanced Energy Materials* **2023**, *13*, 2301670.

[47] G. Duan, Y. Wang, B. Luo, L. Sun, S. Zheng, J. Huang, Z. Ye, *Energy Storage Materials* **2023**, *61*, 102882.

[48] Z. Zhang, Y. Zhang, M. Ye, Z. Wen, Y. Tang, X. Liu, C. C. Li, *Angew Chem Int Ed* **2023**, *62*, e202311032.

[49] L. Liu, H. Lu, C. Han, X. Chen, S. Liu, J. Zhang, X. Chen, X. Wang, R. Wang, J. Xu, H. K. Liu, S. X. Dou, W. Li, *ACS Nano* **2023**, *17*, 23065–23078.

[50] X. Zhang, Z. Deng, C. Xu, Y. Deng, Y. Jia, H. Luo, H. Wu, W. Cai, Y. Zhang, *Advanced Energy Materials* **2023**, 2302749.

[51] T. Wu, C. Hu, Q. Zhang, Z. Yang, G. Jin, Y. Li, Y. Tang, H. Li, H. Wang, *Adv Funct Materials* **2024**, 2315716.

[52] Y. Ding, L. Yin, T. Du, Y. Wang, Z. He, J. A. Yuwono, G. Li, J. Liu, S. Zhang, T. Yang, Z. Guo, *Adv Funct Materials* **2024**, 2314388.

[53] A. Zhou, H. Wang, F. Zhang, X. Hu, Z. Song, Y. Chen, Y. Huang, Y. Cui, Y. Cui, L. Li, F. Wu, R. Chen, *Nano-Micro Lett.* **2024**, *16*, 164.

[54] S. Zhou, X. Meng, Y. Chen, J. Li, S. Lin, C. Han, X. Ji, Z. Chang, A. Pan, *Angew Chem Int Ed* **2024**, e202403050.

[55] Q. Guo, G. Teri, W. Mo, J. Huang, F. Liu, M. Ye, D. Fu, *Energy Environ. Sci.* **2024**, 10.1039.D4EE00986J.

[56] Y. Yang, Y. Li, Q. Zhu, B. Xu, *Adv Funct Materials* **2024**, 2316371.

[57] J. Zhang, Y. Liu, Y. Wang, Z. Zhu, Z. Yang, *Adv Funct Materials* **2024**, 2401889.

[58] L. Deng, X. Xie, W. Song, A. Pan, G. Cao, S. Liang, G. Fang, *Chemical Engineering Journal* **2024**, *488*, 151104.

[59] R. Huang, J. Zhang, W. Wang, X. Wu, X. Liao, T. Lu, Y. Li, J. Chen, S. Chen, Y. Qiao, Q. Zhao, H. Wang, *Energy Environ. Sci.* **2024**, 10.1039.D4EE00109E.

[60] J. Dong, L. Su, H. Peng, D. Wang, H. Zong, G. Wang, J. Yang, *Angew Chem Int Ed* **2024**, e202401441.

[61] M. Chen, J. Zhang, X. Ji, J. Fu, G. Feng, *Current Opinion in Electrochemistry* **2022**, *34*, 101030.

[62] W. M. Khairul, R. Rahamathullah, J. R. Joni, M. I. N. Isa, *International Journal of Hydrogen Energy* **2022**, *47*, 27866–27876.

[63] S. Silvarajoo, U. M. Osman, K. H. Kamarudin, M. H. Razali, H. M. Yusoff, I. U. H. Bhat, M. Z. H. Rozaini, Y. Juahir, *Data in Brief* **2020**, *32*, 106299.

[64] J. Wan, R. Wang, Z. Liu, L. Zhang, F. Liang, T. Zhou, S. Zhang, L. Zhang, Q. Lu, C. Zhang, Z. Guo, *ACS Nano* **2023**, *17*, 1610–1621.

[65] X. Gan, J. Tang, X. Wang, L. Gong, I. Zhitomirsky, L. Qie, K. Shi, *Energy Storage Materials* **2023**, *59*, 102769.

[66] Z. Zhao, P. Li, Z. Zhang, H. Zhang, G. Li, *Chemical Engineering Journal* **2023**, *454*, 140435.

[67] Z. Cheng, K. Wang, J. Fu, F. Mo, P. Lu, J. Gao, D. Ho, B. Li, H. Hu, *Advanced Energy Materials* **2024**, 2304003.

[68] F. Pflüger, B. Hernández, M. Ghomi, *J. Phys. Chem. B* **2010**, *114*, 9072–9083.

[69] B. Hernández, F. Pflüger, N. Derbel, J. De Coninck, M. Ghomi, *J. Phys. Chem. B* **2010**, *114*, 1077–1088.

[70] X. Yu, Z. Li, X. Wu, H. Zhang, Q. Zhao, H. Liang, H. Wang, D. Chao, F. Wang, Y. Qiao, H. Zhou, S.-G. Sun, *Joule* **2023**, *7*, 1145–1175.

[71] Q. Li, A. Chen, D. Wang, Y. Zhao, X. Wang, X. Jin, B. Xiong, C. Zhi, *Nat Commun* **2022**, *13*, 3699.